CWP-1014

# Angular and Modal Equipartitioning of Elastic Waves in Scattering Media: A Numerical Study Based on Energy Transport

Manuel Jaimes and Roel Snieder

*Center for Wave Phenomena, Colorado School of Mines, Golden, CO 80401, USA*

(Dated: 7 February 2023)

We illustrate the angular and modal equipartitioning of elastic waves in scattering media using the elastic radiative transfer equations in 2-D. To solve these equations we decompose the $P$ and $S$ specific intensities into direct and scattered components. We handle the direct component analytically, and derive integral equations for the scattered components of the $P$ and $S$ specific intensities. We construct a time-stepping algorithm with which we evolve the scattered components of the specific intensities numerically in time. We handle the advection of $P$ and $S$ energy analytically at the computational grid points and use numerical interpolation to deal with advection terms which do not lie on the grid points. This approach allows us to reduce numerical dispersion, compared to standard numerical techniques. We test this algorithm for a pure $P$ source, and a double couple which radiates both $P$ and $S$ energy. We compare our numerical solutions against known approximations, and find good agreement. We use this algorithm to numerically study the local behavior of equipartitioning over wave modes and angular directions. We find that both types of equipartitioning are a function of space and time, depending on the extent of scattering. This local behavior must be taken into account when studying diffusion and equipartitioning of elastic waves.

## I. INTRODUCTION

As waves propagate through a scattering medium they lose (or gain) energy due to scattering to (or from) other directions. When dealing with elastic waves the scattering also accounts for mode conversion. In the absence of anelastic attenuation, scattering and mode conversion obey energy conservation, which one may mathematically describe using the radiative transfer equations (RTE). The RTE consist of a coupled system of integro-differential equations where one solves for the wave intensity as a function of space, time, and angular direction (and wave mode if dealing with elastic waves), assuming one knows the scattering mean free path(s), the angular dependence of the scattering pattern(s), and the speed(s) of energy propagation. Both acoustic and elastic formulations to the RTE have been studied (Gaebler *et al.*, 2015; Margerin *et al.*, 2016; Zhang and Sens-Schönfelder, 2022), with most of the attention devoted to the acoustic formulation. The elastic formulation is harder to study than the acoustic formulation, because there is coupling not only in the angular direction but also in the mode of propagation due to $P \rightarrow S$ and $S \rightarrow P$ mode conversions. In 2-D the acoustic RTE consists of a coupled system of $N$ equations, where $N$ refers to number of angular directions. In contrast, in 2-D the elastic RTE consists of a coupled system of $2N$ equations. In 3-D the elastic RTE consists of a coupled system of $5NM$ equations, where the factor of five corresponds to the size of the stokes vector, $N$ is the number of angular directions in the azimuthal plane and $M$ is the number of angular directions in the polar plane (Turner and Weaver, 1994).

The acoustic description to RTE has been used in astrophysics to analyze radiation transport across cosmic dust in a wide range of astrophysical objects (Steinacker *et al.*, 2002; Narayanan *et al.*, 2021; Wolf, 2003); in atmospheric sciences to model solar radiation across clouds to better understand the evolution of sea surface temperatures (Evans and Stephens, 1995; Aumann *et al.*, 2018; Manners *et al.*, 2009); in optics to develop novel optical tomographic imaging algorithms which allow diagnosis and treatment of biological tissues (Klose *et al.*, 2002; Abdoulaev, 2003; Ren *et al.*, 2004; Yodh and Chance, 1995); in acoustics to model the interaction of acoustic waves with the ocean bottom (Quijano and Zurk, 2009), forest acoustics (Ostashev *et al.*, 2017), and acoustical diffractions by obstacles (Reboul *et al.*, 2005); in geophysics to model infrared radiation across volcanic ash clouds (Prata, 1989; Francis *et al.*, 2012; Lee *et al.*, 2014), heat transfer in the mantle (Hofmeister, 2005), and scattering kernels in coda wave interferometry (Pacheco and Snieder, 2005; Rossetto *et al.*, 2011; Margerin *et al.*, 2016; Snieder *et al.*, 2019; Duran *et al.*, 2020; Dinther *et al.*, 2021; Obermann *et al.*, 2016). Several numerical techniques have been developed to solve the acoustic RTE. These include the Discontinuous Galerkin finite element method (Clarke *et al.*, 2019; Han *et al.*, 2010); Markov Chain Monte Carlo (Iwabuchi, 2006; Xu *et al.*, 2011; Camps and Baes, 2018; Noebauer and Sim, 2019; Przybilla and Korn, 2008; Yoshimoto, 2000); Finite Difference (Klose and Hielscher, 1999); and Wave Equation modeling, whereby one exploits the connection between the acoustic wave equation and the acoustic RTE (Przybilla *et al.*, 2006; Kanu and Snieder, 2015; Snieder *et al.*, 2019; Duran *et al.*, 2020). In addition to these numerical techniques, several authors have derived analytical approximations to the acoustic RTE. These approximations include assuming a point-like, isotropic, impulsive source of

intensity in a statistically homogeneous medium (Margerin *et al.*, 2016); expanding the intensity and scattering function into a finite sum of Legendre polynomial and then solving a finite system of equations for the unknown coefficients appearing in a truncated expansion (Roberge, 1983); decomposing the specific intensities into a sum of partial intensities and then solving the RTE for each partial intensity assuming that scattering is angle-independent and that the source is isotropic (Paasschens, 1997); assuming a steady-state intensity field (Fan *et al.*, 2019; Le Hardy *et al.*, 2016); assuming azimuthal symmetry (Baes and Dejonghe, 2001; de Abreu, 2004); or assuming that the wave propagation is diffusive, which is only valid at times much larger than the transport mean free time (Rossetto *et al.*, 2011; Planès *et al.*, 2014).

The elastic formulation to the RTE has been mostly restricted to seismology. Wu and Aki (1985) introduce the RTE in seismology to describe the generation of seismic coda as seismic waves scatter through the heterogeneous Earth's structure. Sato *et al.* (1997) use RTE to derive semi-analytical expressions of the energy density due to a point shear-dislocation source. Margerin *et al.* (2000) use Monte Carlo simulations to study the multiple scattering of elastic waves via the elastic RTE. Przybilla *et al.* (2006) solve the elastic RTE using a Monte Carlo method and compare their results to finite difference modeling of elastic waves in a 2-D random medium. Yamamoto and Sato (2010) use radiative transfer theory to study multiple scattering and mode conversions of seismic waves at Asama volcano in Japan. For a thorough overview of the analytical, numerical, and applied aspects of both the acoustic and elastic RTE we refer the reader to Sato *et al.* (2012). The elastic RTE has also been used to study the late time behavior of elastic waves. At late times, after many scattering events, the

ratio of $S$ to $P$ energy equals a constant which depends on the $P$ and $S$ wave mean velocities and the dimension under consideration (Weaver, 1982; Snieder, 2002). Similarly, at late times, the angular distribution of the $P$ and $S$ energy homogenizes (Margerin *et al.*, 2000). This late time behavior is usually referred to as the equipartitioned state of elastic waves. Khazaie *et al.* (2017) numerically studied the transition to the equipartitioned state in a randomly heterogeneous elastic medium for a wide range of modeling parameters. Sánchez-Sesma *et al.* (2008) theoretically studied equipartitioning as a necessary condition for the retrieval of Green's functions in seismic inteferometry. Hennino *et al.* (2001) investigated the principle of equipartitioning using observational data of seismic coda. In this paper we refer to the equilibration of energy between $P$ and $S$ modes as modal equipartitioning, and the homogenization along the angular direction as angular equipartitioning.

Most studies have only considered the global behavior (i.e., time dependence without regard of spatial location) of the modal equipartitioning. In this paper we investigate both the local and global behavior of the modal and angular equipartitioning. The paper is organized as follows: In section 2 we provide a description of the elastic RTE, and derive a time-stepping algorithm based on an integral equation formalism that allows us to compute the spatio-temporal-angular distribution of the $P$ and $S$ energies. In section 3, we show numerical simulations for an explosive source which radiates $P$ waves, and a double couple source which radiates $P$ and $S$ waves. We study the local and global behavior of equipartitioning for both of these sources. In section 4 we discuss our findings. In appendix A we show the diffusive approximation that we use to benchmark our algorithm. In appendix B we show the analytical expressions for the total $P$ and $S$ energies which we

compare against our numerical results in section 3. In appendix C we show how we make our numerical scheme energy conserving.

## II. THEORY

### A. Description of the Elastic Radiative Transfer Equations

The two dimensional elastic radiative transfer equations correspond to the following coupled system of equations (Zhang *et al.*, 2021)

$$\frac{\partial I^P(\mathbf{r},\hat{\mathbf{n}},t)}{\partial t} + \alpha_0\hat{\mathbf{n}}\cdot\nabla I^P(\mathbf{r},\hat{\mathbf{n}},t) = -\alpha_0(g^0_{pp}+g^0_{ps})I^P(\mathbf{r},\hat{\mathbf{n}},t) + \alpha_0\oint g_{pp}(\hat{\mathbf{n}},\hat{\mathbf{n}}')I^P(\mathbf{r},\hat{\mathbf{n}}',t)d^2\hat{\mathbf{n}}' + \beta_0\oint g_{sp}(\hat{\mathbf{n}},\hat{\mathbf{n}}')I^S(\mathbf{r},\hat{\mathbf{n}}',t)d^2\hat{\mathbf{n}}', \tag{1}$$

$$\frac{\partial I^S(\mathbf{r},\hat{\mathbf{n}},t)}{\partial t} + \beta_0\hat{\mathbf{n}}\cdot\nabla I^S(\mathbf{r},\hat{\mathbf{n}},t) = -\beta_0(g^0_{ss}+g^0_{sp})I^S(\mathbf{r},\hat{\mathbf{n}},t) + \beta_0\oint g_{ss}(\hat{\mathbf{n}},\hat{\mathbf{n}}')I^S(\mathbf{r},\hat{\mathbf{n}}',t)d^2\hat{\mathbf{n}}' + \alpha_0\oint g_{ps}(\hat{\mathbf{n}},\hat{\mathbf{n}}')I^P(\mathbf{r},\hat{\mathbf{n}}',t)d^2\hat{\mathbf{n}}', \tag{2}$$

where the superscripts $P$ and $S$ indicate the specific intensity of the $P$ and $S$-waves, respectively. In eqns. 1 and 2 we ignore intrinsic attenuation, and $\alpha_0$ and $\beta_0$ describe the mean propagation velocity of $P$ and $S$ waves, respectively. The terms $\hat{\mathbf{n}}' = (\cos\gamma', \sin\gamma')$ and $\hat{\mathbf{n}} = (\cos\gamma, \sin\gamma)$, with $\gamma'$(or $\gamma$) the angle relative to the positive $x-$direction, denote the incident and scattered propagation directions, respectively, while $\nabla = (\partial/\partial x, \partial/\partial y)$ denotes the gradient operator. The terms $g_{ij}(\hat{\mathbf{n}},\hat{\mathbf{n}}')$, with $\{i,j = p,s\}$, denote the scattering functions, which describe scattering between different angles and mode conversion. They

quantify the energy transfer from a wave of mode $i$ incident in direction $\hat{\mathbf{n}}'$ to a wave that scatters as a mode $j$ towards direction $\hat{\mathbf{n}}$. These scattering functions assume that scattering only depends on $\hat{\mathbf{n}}' \cdot \hat{\mathbf{n}} = \cos\theta$, where $\theta$ is the angle between the incident and scattered directions. Therefore, $\theta = 0$ corresponds to forward scattering, and $\theta = \pi$ corresponds to backward scattering. The terms $g_{ij}^0$ denote the total scattering coefficients and are defined as $g_{ij}^0 = \oint g_{ij}(\theta) d\theta$. They describe the energy transfer from a wave of mode $i$ to a wave of mode $j$. The left-hand side of eqns. 1 and 2 describe the advection of the $P$ and $S$ specific intensities, respectively. The first term on the right-hand side of eqns. 1 and 2 describes scattering losses due to scattering to other angles and mode conversion. The integral terms describe energy gain due to scattering from other angles and mode conversion. Equations 1 and 2 follow from the ladder approximation to the Bethe-Salpeter equation assuming that $ka\epsilon \ll 1$, where $k$ is the wavenumber, and $a, \epsilon^2$ are the correlation length and variance of the random medium, respectively Przybilla *et al.* (2006). In this paper we refer to $I^m(\mathbf{r}, \hat{\mathbf{n}}, t)$ as the *specific intensity*, $E^m(\mathbf{r}, t) = \oint I^m(\mathbf{r}, \hat{\mathbf{n}}, t) d^2\hat{\mathbf{n}}$ as the *energy density*, and $Y^m(t) = \int E^m(\mathbf{r}, t) dxdy$ as the *total energy*. The superscript $m$ indicates $P$ or $S$ wave mode.

For late times, when the wave propagation is almost independent of direction, and is nearly stationary in time, the elastic RTE equations 1 and 2 lead to diffusive wave transport (Sato *et al.*, 2012). The conventional diffusion approximation to the elastic RTE describes the spatio-temporal evolution of the combined energy density $E(\mathbf{r}, t) = E^P(\mathbf{r}, t) + E^S(\mathbf{r}, t)$. Describing the energies $E^P$ and $E^S$ independently of each other is not possible due to the coupling between wave modes (Trégourès and van Tiggelen, 2002). In the diffusive regime, after enough scattering events, the ratio of the total energy carried by $S$ waves, to that

carried by $P$ waves, is $2(\alpha_0/\beta_0)^3$ in 3-D (Weaver, 1982; Snieder, 2002) and $(\alpha_0/\beta_0)^2$ in 2-D (Zhang *et al.*, 2021). Despite the coupling between wave modes, one can derive expressions for the total energy, rather than the energy density, carried by the $P$ and $S$ waves. Sato *et al.* (2012) give expressions for the evolution of the total energies $Y^P(t)$ and $Y^S(t)$. To do this, they assume the source is isotropic, that the $P$ and $S$ specific intensities are almost isotropic, and that the spatial gradient of the $P$ and $S$ energy densities vanishes at large distances. With some modifications their expressions are also valid for non-isotropic sources, under the requirement that the spatial gradient of the $P$ and $S$ specific intensities vanishes at large distances from the source, as we show in Appendix B. The rate at which $Y^P(t)$ and $Y^S(t)$ vary over time is only a function of the scattering properties of the medium.

### B. Formulation of the Time-Stepping Algorithm

We solve the system of eqns. 1 and 2, with the $P$ and $S$ specific intensities subject to the following initial conditions

$$I^P(\mathbf{r}, \hat{\mathbf{n}}, t = t_0) = I_0^P(\mathbf{r}, \hat{\mathbf{n}}),$$
$$I^S(\mathbf{r}, \hat{\mathbf{n}}, t = t_0) = I_0^S(\mathbf{r}, \hat{\mathbf{n}}). \tag{3}$$

We carry out the simulation for times less than the propagation time for a $P$-wave to reach the boundary. In such case, the boundary values do not affect the simulation, as long as no energy is injected into the computational domain from the boundary. We decompose the specific intensities into the direct and scattered components

$$I^P(\mathbf{r},\hat{\mathbf{n}},t) = I^P_{dir}(\mathbf{r},\hat{\mathbf{n}},t) + I^P_{scat}(\mathbf{r},\hat{\mathbf{n}},t),$$

$$I^S(\mathbf{r},\hat{\mathbf{n}},t) = I^S_{dir}(\mathbf{r},\hat{\mathbf{n}},t) + I^S_{scat}(\mathbf{r},\hat{\mathbf{n}},t). \tag{4}$$

Similarly, we decompose the initial conditions in eqn. 3

$$I^P_{dir}(\mathbf{r},\hat{\mathbf{n}},t=t_0) = I^P_0(\mathbf{r},\hat{\mathbf{n}}); I^P_{scat}(\mathbf{r},\hat{\mathbf{n}},t=t_0) = 0,$$

$$I^S_{dir}(\mathbf{r},\hat{\mathbf{n}},t=t_0) = I^S_0(\mathbf{r},\hat{\mathbf{n}}); I^S_{scat}(\mathbf{r},\hat{\mathbf{n}},t=t_0) = 0, \tag{5}$$

where the subscripts *dir* and *scat* denote the direct and scattered parts of the specific intensity, respectively. This decomposition allows us to reduce numerical errors since the direct component of the specific intensity can be handled analytically. The direct components of the $P$ and $S$ specific intensities satisfy

$$\frac{\partial I^P_{dir}(\mathbf{r},\hat{\mathbf{n}},t)}{\partial t} + \alpha_0\hat{\mathbf{n}}\cdot\nabla I^P_{dir}(\mathbf{r},\hat{\mathbf{n}},t) = -\alpha_0(g^0_{pp}+g^0_{ps})I^P_{dir}(\mathbf{r},\hat{\mathbf{n}},t), \tag{6}$$

and

$$\frac{\partial I^S_{dir}(\mathbf{r},\hat{\mathbf{n}},t)}{\partial t} + \beta_0\hat{\mathbf{n}}\cdot\nabla I^S_{dir}(\mathbf{r},\hat{\mathbf{n}},t) = -\beta_0(g^0_{ss}+g^0_{sp})I^S_{dir}(\mathbf{r},\hat{\mathbf{n}},t), \tag{7}$$

respectively. The exact solutions to eqns. 6 and 7, for the initial conditions in 5, are

$$I^P_{dir}(\mathbf{r},\hat{\mathbf{n}},t) = I^P_{dir}(\mathbf{r}-\alpha_0(t-t_0)\hat{\mathbf{n}},\hat{\mathbf{n}},t=t_0)e^{-\alpha_0(g^0_{pp}+g^0_{ps})(t-t_0)}, \tag{8}$$

and

$$I^S_{dir}(\mathbf{r},\hat{\mathbf{n}},t) = I^S_{dir}(\mathbf{r}-\beta_0(t-t_0)\hat{\mathbf{n}},\hat{\mathbf{n}},t=t_0)e^{-\beta_0(g^0_{ss}+g^0_{sp})(t-t_0)}. \tag{9}$$

Inserting the decomposition in eqn. 4 into eqns. 1 and 2, with the help of eqns. 6 and 7, gives

$$\frac{\partial I^P_{scat}(\mathbf{r},\hat{\mathbf{n}},t)}{\partial t} + \alpha_0\hat{\mathbf{n}}\cdot\nabla I^P_{scat}(\mathbf{r},\hat{\mathbf{n}},t) = -\alpha_0(g^0_{pp}+g^0_{ps})I^P_{scat}(\mathbf{r},\hat{\mathbf{n}},t) + \alpha_0\oint g_{pp}(\hat{\mathbf{n}},\hat{\mathbf{n}}')I^P(\mathbf{r},\hat{\mathbf{n}}',t)d^2\hat{\mathbf{n}}' + \beta_0\oint g_{sp}(\hat{\mathbf{n}},\hat{\mathbf{n}}')I^S(\mathbf{r},\hat{\mathbf{n}}',t)d^2\hat{\mathbf{n}}', \tag{10}$$

$$\frac{\partial I^S_{scat}(\mathbf{r},\hat{\mathbf{n}},t)}{\partial t} + \beta_0\hat{\mathbf{n}}\cdot\nabla I^S_{scat}(\mathbf{r},\hat{\mathbf{n}},t) = -\beta_0(g^0_{ss}+g^0_{sp})I^S_{scat}(\mathbf{r},\hat{\mathbf{n}},t) + \beta_0\oint g_{ss}(\hat{\mathbf{n}},\hat{\mathbf{n}}')I^S(\mathbf{r},\hat{\mathbf{n}}',t)d^2\hat{\mathbf{n}}' + \alpha_0\oint g_{ps}(\hat{\mathbf{n}},\hat{\mathbf{n}}')I^P(\mathbf{r},\hat{\mathbf{n}}',t)d^2\hat{\mathbf{n}}'. \tag{11}$$

Note that in eqns. 10 and 11 the integral contributions still contain the total specific intensity for each of the modes. Using the work of Paasschens (1997) we transform eqns. 10 and 11 into the following integral equations

$$I^P_{scat}(\mathbf{r},\hat{\mathbf{n}},t) = I^P_{scat}(\mathbf{r}-\alpha_0(t-t_0)\hat{\mathbf{n}},\hat{\mathbf{n}},t_0)e^{-(t-t_0)\alpha_0(g^0_{pp}+g^0_{ps})} + \int_{t_0}^{t}\oint\Big[\alpha_0 g_{pp}(\hat{\mathbf{n}},\hat{\mathbf{n}}')I^P(\mathbf{r}-\alpha_0(t-t')\hat{\mathbf{n}},\hat{\mathbf{n}}',t') + \beta_0 g_{sp}(\hat{\mathbf{n}},\hat{\mathbf{n}}')I^S(\mathbf{r}-\alpha_0(t-t')\hat{\mathbf{n}},\hat{\mathbf{n}}',t')\Big]e^{-(t-t')\alpha_0(g^0_{pp}+g^0_{ps})}d^2\hat{\mathbf{n}}'dt', \tag{12}$$

$$I^S_{scat}(\mathbf{r},\hat{\mathbf{n}},t) = I^S_{scat}(\mathbf{r}-\beta_0(t-t_0)\hat{\mathbf{n}},\hat{\mathbf{n}},t_0)e^{-(t-t_0)\beta_0(g^0_{ss}+g^0_{sp})} + \int_{t_0}^{t}\oint\Big[\beta_0 g_{ss}(\hat{\mathbf{n}},\hat{\mathbf{n}}')I^S(\mathbf{r}-\beta_0(t-t')\hat{\mathbf{n}},\hat{\mathbf{n}}',t') + \alpha_0 g_{ps}(\hat{\mathbf{n}},\hat{\mathbf{n}}')I^P(\mathbf{r}-\beta_0(t-t')\hat{\mathbf{n}},\hat{\mathbf{n}}',t')\Big]e^{-(t-t')\beta_0(g^0_{ss}+g^0_{sp})}d^2\hat{\mathbf{n}}'dt'. \tag{13}$$

159 Paasschens (1997) analytically solve for the specific intensities in the acoustic version
160 of equation 12 (i.e., they disregard the terms involving conversion from $P$ to $S$ waves)
161 for a medium with isotropic scattering and constant scattering properties assuming that the
162 initial condition for the specific intensity is isotropic. To do this, they decompose the specific
163 intensities into a sum of partial intensities, where each partial intensity signifies a number of
164 scattering events (i.e., direct propagation, single scattering, double scattering, and so on). In
165 equations 12 and 13 we deal with the advection of the specific intensities exactly at the grid
166 points, and through interpolation at points that lie within the grid points. This approach
167 allows us to reduce the numerical dispersion, compared to standard numerical techniques.
168 In this paper we use equation 12 and 13 to integrate the specific intensities numerically
169 in time. This procedure allows us to use non-isotropic initial conditions and non-isotropic
170 scattering radiation patterns.

171 To develop a time-stepping algorithm which depends only on the current time $t$, and the
172 previous time $t - \Delta t$, we replace $t_0$ by $t - \Delta t$ to obtain

$$
\begin{aligned}
I^P_{scat}(\mathbf{r}, \hat{\mathbf{n}}, t) = {} & I^P_{scat}(\mathbf{r} - \alpha_0 \Delta t \hat{\mathbf{n}}, \hat{\mathbf{n}}, t - \Delta t) e^{-\Delta t \alpha_0 (g^0_{pp} + g^0_{ps})} \\
& + \int_{t-\Delta t}^{t} \oint \Big[ \alpha_0 g_{pp}(\hat{\mathbf{n}}, \hat{\mathbf{n}}') I^P(\mathbf{r} - \alpha_0 (t - t') \hat{\mathbf{n}}, \hat{\mathbf{n}}', t') \\
& + \beta_0 g_{sp}(\hat{\mathbf{n}}, \hat{\mathbf{n}}') I^S(\mathbf{r} - \alpha_0 (t - t') \hat{\mathbf{n}}, \hat{\mathbf{n}}', t') \Big] e^{-(t-t')\alpha_0 (g^0_{pp} + g^0_{ps})} d^2 \hat{\mathbf{n}}' dt', \qquad (14)
\end{aligned}
$$

$$I^S_{scat}(\mathbf{r},\hat{\mathbf{n}},t) = I^S_{scat}(\mathbf{r}-\beta_0\Delta t\hat{\mathbf{n}},\hat{\mathbf{n}},t-\Delta t)e^{-\Delta t\beta_0(g^0_{ss}+g^0_{sp})}$$
$$+ \oint\int_{t-\Delta t}^{t}\Big[\beta_0 g_{ss}(\hat{\mathbf{n}},\hat{\mathbf{n}}')I^S(\mathbf{r}-\beta_0(t-t')\hat{\mathbf{n}},\hat{\mathbf{n}}',t')$$
$$+ \alpha_0 g_{ps}(\hat{\mathbf{n}},\hat{\mathbf{n}}')I^P(\mathbf{r}-\beta_0(t-t')\hat{\mathbf{n}},\hat{\mathbf{n}}',t')\Big]e^{-(t-t')\beta_0(g^0_{ss}+g^0_{sp})}d^2\hat{\mathbf{n}}'dt'. \quad (15)$$

We proceed by applying the discrete ordinate method (Chandrasekhar, 1960) whereby one divides the angular integral into $N$ equal segments. In two dimensions this method corresponds to setting $d^2\hat{\mathbf{n}} \to d\theta$ and then setting $d\theta = 2\pi/N$ in the angular integration

$$I^P_{scat}(\mathbf{r},\hat{\mathbf{n}},t) = I^P_{scat}(\mathbf{r}-\alpha_0\Delta t\hat{\mathbf{n}},\hat{\mathbf{n}},t-\Delta t)e^{-\Delta t\alpha_0(g^0_{pp}+g^0_{ps})}$$
$$+ \frac{2\pi}{N}\int_{t-\Delta t}^{t}\sum_{\hat{\mathbf{n}}'}\Big[\alpha_0 g_{pp}(\hat{\mathbf{n}},\hat{\mathbf{n}}')I^P(\mathbf{r}-\alpha_0(t-t')\hat{\mathbf{n}},\hat{\mathbf{n}}',t')$$
$$+ \beta_0 g_{sp}(\hat{\mathbf{n}},\hat{\mathbf{n}}')I^S(\mathbf{r}-\alpha_0(t-t')\hat{\mathbf{n}},\hat{\mathbf{n}}',t')\Big]e^{-(t-t')\alpha_0(g^0_{pp}+g^0_{ps})}dt', \quad (16)$$

$$I^S_{scat}(\mathbf{r},\hat{\mathbf{n}},t) = I^S_{scat}(\mathbf{r}-\beta_0\Delta t\hat{\mathbf{n}},\hat{\mathbf{n}},t-\Delta t)e^{-\Delta t\beta_0(g^0_{ss}+g^0_{sp})}$$
$$+ \frac{2\pi}{N}\int_{t-\Delta t}^{t}\sum_{\hat{\mathbf{n}}'}\Big[\beta_0 g_{ss}(\hat{\mathbf{n}},\hat{\mathbf{n}}')I^S(\mathbf{r}-\beta_0(t-t')\hat{\mathbf{n}},\hat{\mathbf{n}}',t')$$
$$+ \alpha_0 g_{ps}(\hat{\mathbf{n}},\hat{\mathbf{n}}')I^P(\mathbf{r}-\beta_0(t-t')\hat{\mathbf{n}},\hat{\mathbf{n}}',t')\Big]e^{-(t-t')\beta_0(g^0_{ss}+g^0_{sp})}dt'. \quad (17)$$

We then discretize the remaining time integral using a two-point quadrature rule, with weights not necessarily equal to 1/2, by which we obtain

$$
\begin{aligned}
I^P_{scat}(\mathbf{r},\hat{\mathbf{n}},t) &= I^P_{scat}(\mathbf{r}-\alpha_0\Delta t\hat{\mathbf{n}},\hat{\mathbf{n}},t-\Delta t)e^{-\Delta t\alpha_0(g^0_{pp}+g^0_{ps})} \\
&+ A_p\Delta t\frac{2\pi}{N}\sum_{\hat{\mathbf{n}}'}\Big[\alpha_0 g_{pp}(\hat{\mathbf{n}},\hat{\mathbf{n}}')I^P(\mathbf{r}-\alpha_0\Delta t\hat{\mathbf{n}},\hat{\mathbf{n}}',t-\Delta t) \\
&+ \beta_0 g_{sp}(\hat{\mathbf{n}},\hat{\mathbf{n}}')I^S(\mathbf{r}-\alpha_0\Delta t\hat{\mathbf{n}},\hat{\mathbf{n}}',t-\Delta t)\Big]e^{-\Delta t\alpha_0(g^0_{pp}+g^0_{ps})} \\
&+ B_p\Delta t\frac{2\pi}{N}\sum_{\hat{\mathbf{n}}'}\Big[\alpha_0 g_{pp}(\hat{\mathbf{n}},\hat{\mathbf{n}}')I^P(\mathbf{r},\hat{\mathbf{n}}',t) \\
&+ \beta_0 g_{sp}(\hat{\mathbf{n}},\hat{\mathbf{n}}')I^S(\mathbf{r},\hat{\mathbf{n}}',t)\Big],
\end{aligned}
\tag{18}
$$

$$
\begin{aligned}
I^S_{scat}(\mathbf{r},\hat{\mathbf{n}},t) &= I^S_{scat}(\mathbf{r}-\beta_0\Delta t\hat{\mathbf{n}},\hat{\mathbf{n}},t-\Delta t)e^{-\Delta t\beta_0(g^0_{ss}+g^0_{sp})} \\
&+ A_s\Delta t\frac{2\pi}{N}\sum_{\hat{\mathbf{n}}'}\Big[\beta_0 g_{ss}(\hat{\mathbf{n}},\hat{\mathbf{n}}')I^S(\mathbf{r}-\beta_0\Delta t\hat{\mathbf{n}},\hat{\mathbf{n}}',t-\Delta t) \\
&+ \alpha_0 g_{ps}(\hat{\mathbf{n}},\hat{\mathbf{n}}')I^P(\mathbf{r}-\beta_0\Delta t\hat{\mathbf{n}},\hat{\mathbf{n}}',t-\Delta t)\Big]e^{-\Delta t\beta_0(g^0_{ss}+g^0_{sp})} \\
&+ B_s\Delta t\frac{2\pi}{N}\sum_{\hat{\mathbf{n}}'}\Big[\beta_0 g_{ss}(\hat{\mathbf{n}},\hat{\mathbf{n}}')I^S(\mathbf{r},\hat{\mathbf{n}}',t) \\
&+ \alpha_0 g_{ps}(\hat{\mathbf{n}},\hat{\mathbf{n}}')I^P(\mathbf{r},\hat{\mathbf{n}}',t)\Big].
\end{aligned}
\tag{19}
$$

$A_p$ and $A_s$ denote the lower bound coefficients (corresponding to the intensity at time $t-\Delta t$) in the quadrature rule for the time integral in eqns 16 and 17, respectively. Similarly, $B_p$ and $B_s$ denote the upper bound coefficients (corresponding to the intensity at time $t$) in the quadrature rule. For the trapezoidal quadrature rule that we use in this paper we set $A_p = A_s = B_p = B_s = 1/2$. In the Appendix C we show that this quadrature gives a time-steppping scheme that is energy conserving, as long as the time step $\Delta t$ is much smaller than the scattering mean free time of $P$ and $S$ waves. Eqns. 18 and 19 give the following

system of equations

$$\begin{bmatrix} \boldsymbol{\sigma}^{PP} & \boldsymbol{\sigma}^{SP} \\ \boldsymbol{\sigma}^{PS} & \boldsymbol{\sigma}^{SS} \end{bmatrix} \begin{bmatrix} \vec{I}^{P} \\ \vec{I}^{S} \end{bmatrix} = \begin{bmatrix} \vec{W}^{P} \\ \vec{W}^{S} \end{bmatrix}. \tag{20}$$

where $\vec{I}^{P}, \vec{I}^{S} \in \mathcal{R}^{N\times 1}$ are the solution vectors for the $P$ and $S$ wave intensities, respectively. $\vec{W}^{P}, \vec{W}^{S} \in \mathcal{R}^{N\times 1}$ are

$$\begin{aligned} \vec{W}^{P}(\mathbf{r},\hat{\mathbf{n}},t) &= I^{P}_{scat}(\mathbf{r}-\alpha_0\Delta t\hat{\mathbf{n}},\hat{\mathbf{n}},t-\Delta t)e^{-\Delta t\alpha_0(g^0_{pp}+g^0_{ps})} \\ &+ A_p\Delta t\frac{2\pi}{N}\sum_{\hat{\mathbf{n}}'}\Big[\alpha_0 g_{pp}(\hat{\mathbf{n}},\hat{\mathbf{n}}')I^{P}(\mathbf{r}-\alpha_0\Delta t\hat{\mathbf{n}},\hat{\mathbf{n}}',t-\Delta t) \\ &+ \beta_0 g_{sp}(\hat{\mathbf{n}},\hat{\mathbf{n}}')I^{S}(\mathbf{r}-\alpha_0\Delta t\hat{\mathbf{n}},\hat{\mathbf{n}}',t-\Delta t)\Big]e^{-\Delta t\alpha_0(g^0_{pp}+g^0_{ps})} \\ &+ B_p\Delta t\frac{2\pi}{N}\sum_{\hat{\mathbf{n}}'}\Big[\alpha_0 g_{pp}(\hat{\mathbf{n}},\hat{\mathbf{n}}')I^{P}_{dir}(\mathbf{r},\hat{\mathbf{n}}',t) \\ &+ \beta_0 g_{sp}(\hat{\mathbf{n}},\hat{\mathbf{n}}')I^{S}_{dir}(\mathbf{r},\hat{\mathbf{n}}',t)\Big], \end{aligned} \tag{21}$$

$$\begin{aligned} \vec{W}^{S}(\mathbf{r},\hat{\mathbf{n}},t) &= I^{S}_{scat}(\mathbf{r}-\beta_0\Delta t\hat{\mathbf{n}},\hat{\mathbf{n}},t-\Delta t)e^{-\Delta t\beta_0(g^0_{ss}+g^0_{sp})} \\ &+ A_s\Delta t\frac{2\pi}{N}\sum_{\hat{\mathbf{n}}'}\Big[\beta_0 g_{ss}(\hat{\mathbf{n}},\hat{\mathbf{n}}')I^{S}(\mathbf{r}-\beta_0\Delta t\hat{\mathbf{n}},\hat{\mathbf{n}}',t-\Delta t) \\ &+ \alpha_0 g_{ps}(\hat{\mathbf{n}},\hat{\mathbf{n}}')I^{P}(\mathbf{r}-\beta_0\Delta t\hat{\mathbf{n}},\hat{\mathbf{n}}',t-\Delta t)\Big]e^{-\Delta t\beta_0(g^0_{ss}+g^0_{sp})} \\ &+ B_s\Delta t\frac{2\pi}{N}\sum_{\hat{\mathbf{n}}'}\Big[\beta_0 g_{ss}(\hat{\mathbf{n}},\hat{\mathbf{n}}')I^{S}_{dir}(\mathbf{r},\hat{\mathbf{n}}',t) \\ &+ \alpha_0 g_{ps}(\hat{\mathbf{n}},\hat{\mathbf{n}}')I^{P}_{dir}(\mathbf{r},\hat{\mathbf{n}}',t)\Big]. \end{aligned} \tag{22}$$

We define $\boldsymbol{\sigma}^{PP}$, $\boldsymbol{\sigma}^{SP}$, $\boldsymbol{\sigma}^{PS}$, $\boldsymbol{\sigma}^{SS} \in \mathcal{R}^{N\times N}$ as

$$\begin{aligned} \sigma^{PP}_{ij} &= \delta_{ij} - \alpha_0 B_p\frac{2\pi}{N}\Delta t g_{pp}(\hat{\mathbf{n}}_i,\hat{\mathbf{n}}_j);\ \sigma^{SP}_{ij} = -\beta_0 B_p\frac{2\pi}{N}\Delta t g_{sp}(\hat{\mathbf{n}}_i,\hat{\mathbf{n}}_j) \\ \sigma^{PS}_{ij} &= -\alpha_0 B_s\frac{2\pi}{N}\Delta t g_{ps}(\hat{\mathbf{n}}_i,\hat{\mathbf{n}}_j);\ \sigma^{SS}_{ij} = \delta_{ij} - \beta_0 B_s\frac{2\pi}{N}\Delta t g_{ss}(\hat{\mathbf{n}}_i,\hat{\mathbf{n}}_j). \end{aligned} \tag{23}$$

Directly solving the linear system 20 is expensive. For a computational domain of size $(N_x, N_y, N_t)$, one would need to perform $N_x * N_y * N_t$ linear solves. To speed up the computation we compute the inverse of the matrix

$$\boldsymbol{A} = \begin{bmatrix} \boldsymbol{\sigma}^{PP} & \boldsymbol{\sigma}^{SP} \\ \\ \boldsymbol{\sigma}^{PS} & \boldsymbol{\sigma}^{SS} \end{bmatrix} \tag{24}$$

before-hand via $LU$ decomposition with partial pivoting (chapter 3, Golub and Van Loan, 2013). We quantify the stability of inverting the matrix $\boldsymbol{A}$ in the linear system 20 with the condition number $\kappa(\boldsymbol{A}) = ||\boldsymbol{A}||\ ||\boldsymbol{A}^{-1}||$, where $||\cdot||$ is the 2-norm. When the condition number $\kappa(\boldsymbol{A}) = 1$, the matrix $\boldsymbol{A}$ is well-conditioned. We can control this condition number with the value of the time step $\Delta t$. For the numerical experiments in this paper we have a condition number $\kappa(\boldsymbol{A}) = 1.03$ . We re-write the linear system 20 as

$$\begin{bmatrix} \vec{I}^P \\ \\ \vec{I}^S \end{bmatrix} = \begin{bmatrix} \boldsymbol{\sigma}^{PP} & \boldsymbol{\sigma}^{SP} \\ \\ \boldsymbol{\sigma}^{PS} & \boldsymbol{\sigma}^{SS} \end{bmatrix}^{-1} \begin{bmatrix} \vec{W}^P \\ \\ \vec{W}^S \end{bmatrix}. \tag{25}$$

For the numerical simulations in the next section, we use the scattering functions $g_{pp}, g_{sp}, g_{ps}$ and $g_{ss}$ derived by Zhang *et al.* (2021) for a 2-D exponential random medium. We use $\alpha_0 = 6$ km/s, $\beta_0 = 4$ km/s, and set the correlation distance $a = 0.1$ km, and the variance $\epsilon^2 = 0.0256$. We set the $P$ and $S$ wavenumbers to $k_p = 2\pi v_s/(\lambda_s v_p)$ and $k_s = 2\pi/\lambda_s$, respectively, with $\lambda_s = 1$ km. This choice of parameters gives a scattering mean free time of $\tau_p = 1.36$ s and $\tau_s = 0.82$ s for $P$ and $S$ waves, respectively. We illustrate the angular dependence of these scattering coefficients in fig. 1.

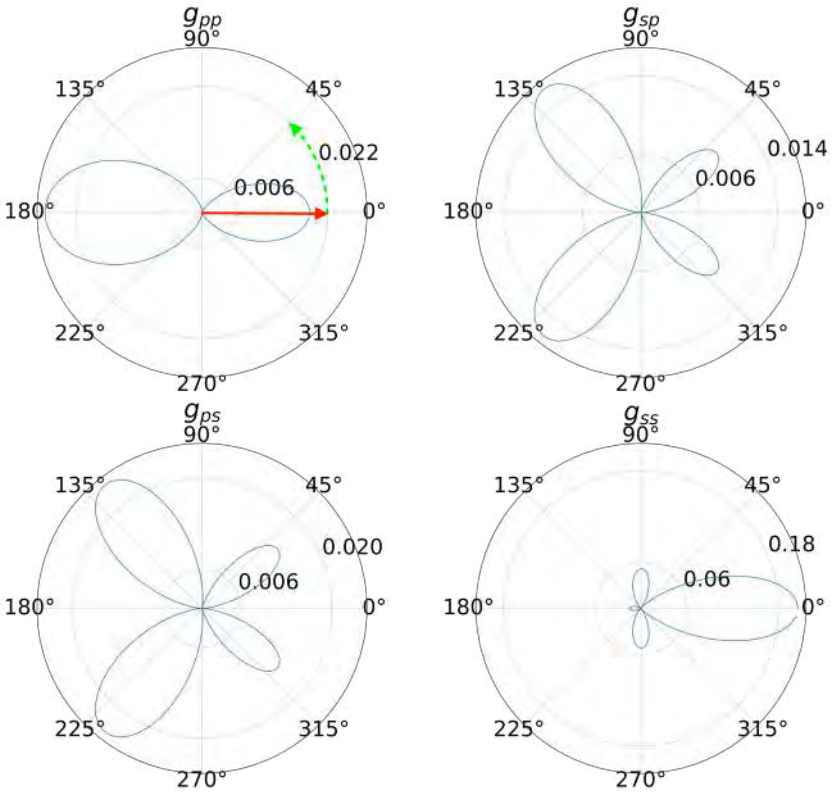


FIG. 1. Polar plots of radiation patterns for an incident wave of mode $i$ propagating along $\theta = 0$, which scatters to mode $j$. The red arrow indicates the incident direction, and the green dashed arrow indicates the direction of increasing scattering angle $\theta$.

## III. NUMERICAL SIMULATIONS

In this section we show numerical simulations for a source which releases only $P$ energy, and a double-couple source which releases both $P$ and $S$ energy. For both simulations we study the local (i.e., function of space and time) and global (i.e., function of time) behavior of modal and angular equipartitioning. For both simulations we use a spatial grid $\Delta x = \Delta y = 1000$ m, with $(x, y) \in [-100, 100]$ km. We use $N = 120$ angular directions. We evolve the$P$ and $S$ specific intensities from $t = 0$ to $T = 16$ s, with $\Delta t = 0.1$ s.

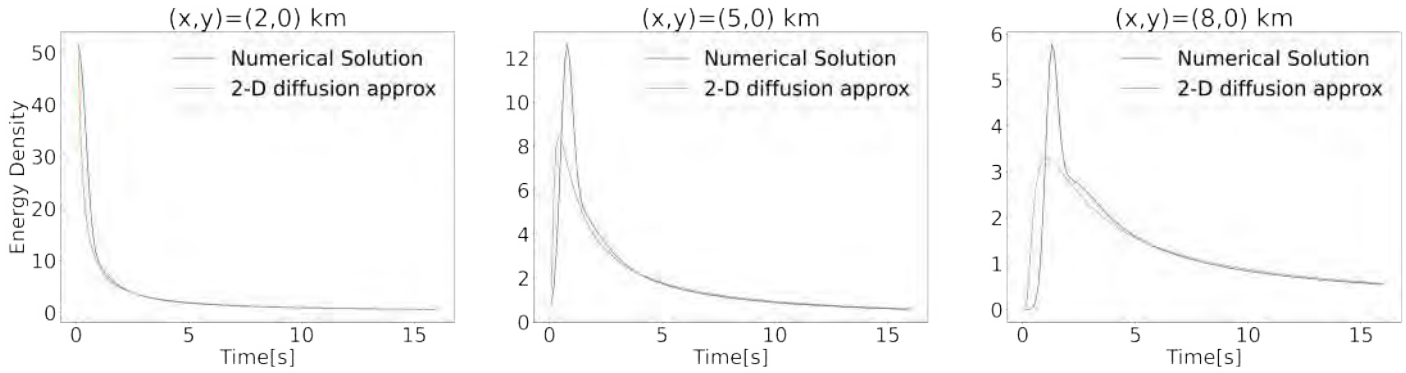


FIG. 2. Comparison of $E(\mathbf{r},t) = E^P(\mathbf{r},t) + E^S(\mathbf{r},t)$ for the pure $P$ source for different distances (shown above in each panel). We compare our numerical solution against the diffusive approximation to the 2-D RTE.

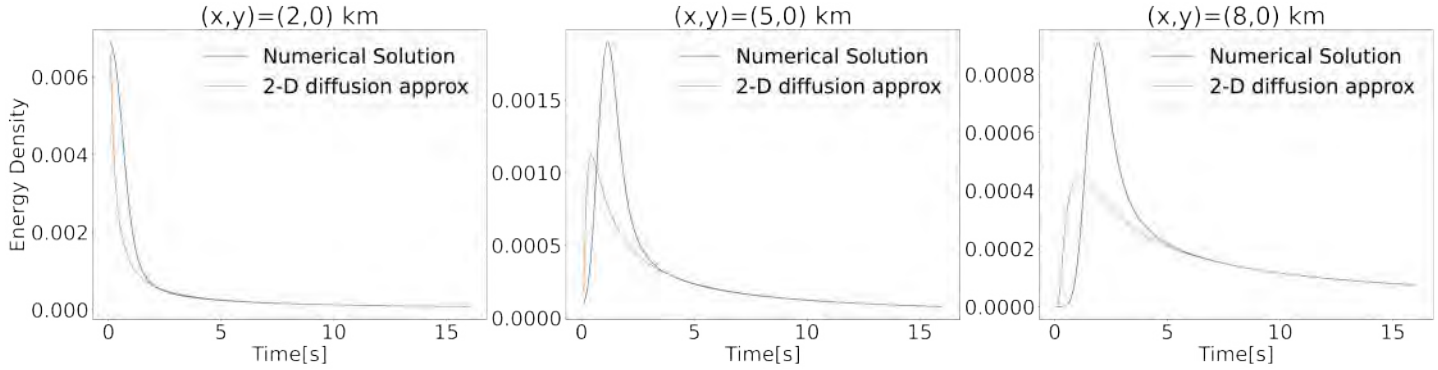


FIG. 3. Comparison of $E(\mathbf{r},t) = E^P(\mathbf{r},t) + E^S(\mathbf{r},t)$ for the double couple source.

### A. Benchmarking of Algorithm

To benchmark the algorithm we use three different tests. First, we compare our numerical solution of the sum of the $P$ and $S$ energy densities, $E(\mathbf{r},t) = E^P(\mathbf{r},t) + E^S(\mathbf{r},t)$, to the diffusive approximation to the 2-D elastic RTE. As mentioned before, the diffusive approximation describes the spatio-temporal evolution of the energy density $E(\mathbf{r},t)$, rather than the individual $P$ and $S$ energy densities. Since most diffusive approximations to the

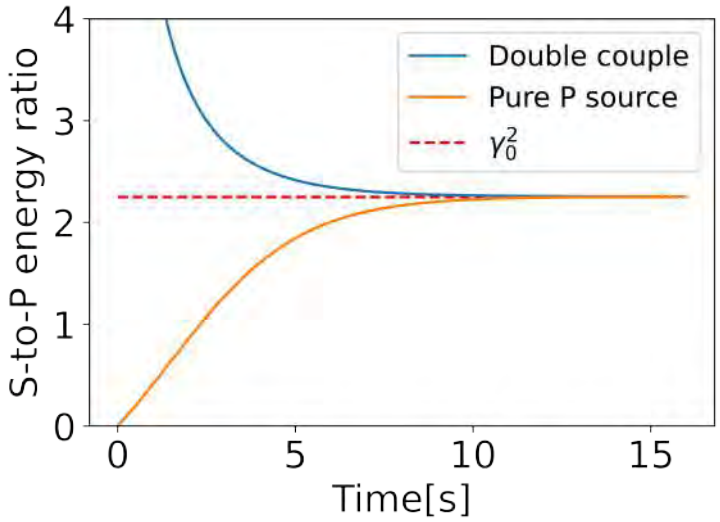


FIG. 4. The ratio $Y^S(t)/Y^P(t)$ for the $P$ source (orange line) and double couple (blue line) simulation. The dashed red line shows the asymptotic ratio $\gamma_0^2 = (\alpha_0/\beta_0)^2$.

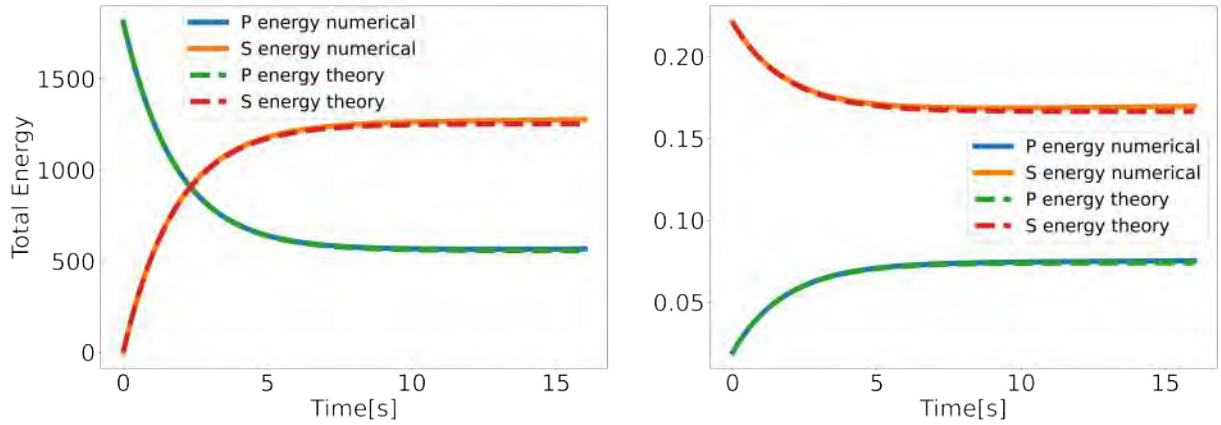


FIG. 5. Comparison of the $P$ and $S$ energies, $Y^P(t)$ and $Y^S(t)$. The blue and orange solid lines show the numerical $P$ and $S$ energy, respectively. The green and red dashed lines show the analytical $P$ and $S$ energy, respectively. The left and right panel show the comparison of the explosive source with a Gaussian extent and double couple source simulations, respectively.

elastic RTE are derived for a 3-D medium, we show in the Appendix A a heuristic 2-D analogous derivation. Second, we compare the global equipartitioning ratio of $S$ to $P$ total energy of our simulations to the theoretical value $(\alpha_0/\beta_0)^2$. This comparison allows us to test the long time behavior of the numerical simulations. Third, we compare the evolution of the $P$ and $S$ energies, $Y^P(t)$ and $Y^S(t)$, of our numerical simulations to analytical expressions. As mentioned before, these expressions are also valid for non-isotropic sources.We center the explosive source around $(x, y) = (0, 0)$ and set the initial condition $I^P_{dir}(\mathbf{r}, \hat{\mathbf{n}}, t = 0) = e^{-r^2/2\sigma^2}$ and $I^S_{dir}(\mathbf{r}, \hat{\mathbf{n}}, t = 0) = 0$, with $\sigma = 1.55\times10^3$ m and $r^2 = x^2+y^2$. For the double couple source we set $I^P_{dir}(\mathbf{r}, \hat{\mathbf{n}}, t = 0) = \sin^2(2\theta)e^{-r^2/2\sigma^2}/\alpha_0^6$, and $I^S_{dir}(\mathbf{r}, \hat{\mathbf{n}}, t = 0) = \cos^2(2\theta)e^{-r^2/2\sigma^2}/\beta_0^6$, with $\theta \in [0, 2\pi]$ and $\sigma = 1.55 \times 10^3$ m. The constants $1/\alpha_0^6$ and $1/\beta_0^6$ correspond to the square of the constants $1/\alpha_0^3$ and $1/\beta_0^3$ appearing in the far-field component of the displacement field in an infinite homogeneous medium due to a double couple radiation pattern (Chapter 4, Aki and Richards, 2009). We evolve the $P$ and $S$ scattered specific intensities using eqn. 25. We compute the direct specific intensities exactly using expressions 8 and 9.

Fig. 2 shows a comparison of the explosive source numerical solution against the 2-D diffusive approximation to RTE for three different distances, $(x, y) = (2, 0), (x, y) = (5, 0)$, and $(x, y) = (8, 0)$ km. Fig. 3 shows the comparison for the double couple source simulation. For all of the panels, in both figs. 2 and 3, our numerical solution matches the diffusive approximation for times much larger than the $P$ and $S$ scattering mean free times ($t \gg \tau_s, \tau_p$). As one goes further away from the source it takes a longer time, relative to points close to the source, for the energy to become diffuse. This explains why, as we go from the left to the middle to the right panel, the solutions only match at late times.

To further test the long time behavior of our algorithm we study the asymptotic behavior of the modal equipartitioning ratio, which converges to $(\alpha_0/\beta_0)^2$ as $t \to \infty$. In practice, this ratio is reached for times much larger than the $P$ and $S$ scattering mean free times ($t \gg \tau_s, \tau_p$). Fig. 4 shows the equipartitioning ratio $Y^S(t)/Y^P(t)$ for both the explosive and double couple source simulations. For times much larger than the $P$ and $S$ scattering times, the numerical ratio converges to the theoretical ratio. This convergence implies a stable long-time behavior of the simulations. For the double couple simulation, the numerical ratio converges to the theoretical ratio slightly faster than for the explosive source simulation. This is because at time $t = 0$ both wave modes carry energy, which speeds up the equilibration of energy. In addition to studying the long time behavior of the energy propagation, we analyze the global distribution of the $P$ and $S$ energies over the whole simulation range $t \in [0, T]$. Fig. 5 shows a comparison of the numerical and analytical evolution of the $P$ and $S$ energies for both the explosive (left panel) and double couple source (right panel) simulation. Overall, our simulation is able to predict the analytical values in the whole simulation range, indicating that the algorithm is accurate. At late times, the numerical solution slightly deviates from analytical values. The accuracy of the solution may be improved by decreasing the value of $\Delta t$.

### B. Local Behavior of Modal Equipartitioning

In 2-D, $\lim_{t\to\infty} Y^S(t)/Y^P(t) = (\alpha_0/\beta_0)^2$, regardless of the source properties (Sato *et al.*, 2012). This ratio is controlled by the repeated conversion between $P$ and $S$ waves, as the energy that is carried by each of the wave modes equilibrates over time. This is shown

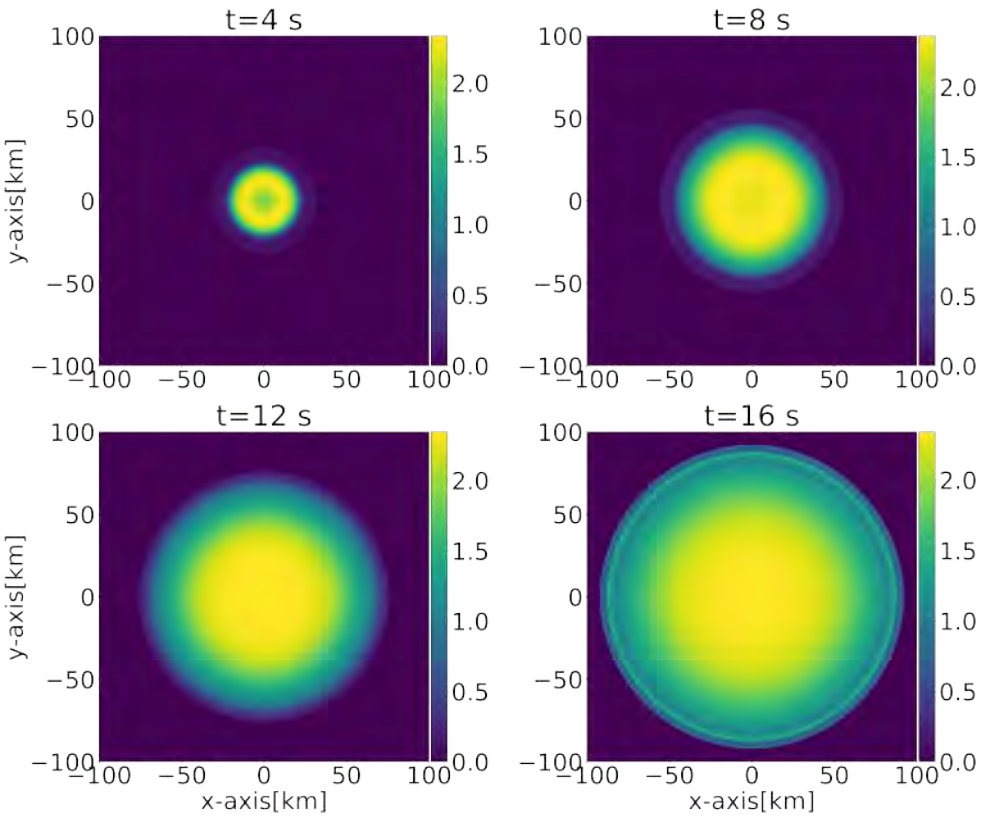


FIG. 6. Snapshots of the local energy ratio $E^S(\mathbf{r},t)/E^P(\mathbf{r},t)$ for the pure $P$ source. This ratio reaches an equilibrium value of 2.34 within the expanding circle in yellow.

by the late time behavior of $Y^P(t)$ and $Y^S(t)$ in fig. 5. Locally, it also follows that $\lim_{t\to\infty} E^S(\mathbf{r},t)/E^P(\mathbf{r},t) = (\alpha_0/\beta_0)^2$ (Sato *et al.*, 2012). Generally speaking, it takes a longer time to reach this local ratio than to reach the global energy ratio. This is because for the local ratio to converge to a constant, regardless of spatial position, the distribution of the energy density must be homogeneous, over space and angular direction, so that the net density flux is zero (i.e., equipartitioned state). In this section we investigate numerically the spatio-temporal dependence of the local ratio. Figs. 6 and 7 show snapshots of the local ratio of the explosive and double couple source simulations, respectively, for simulation times

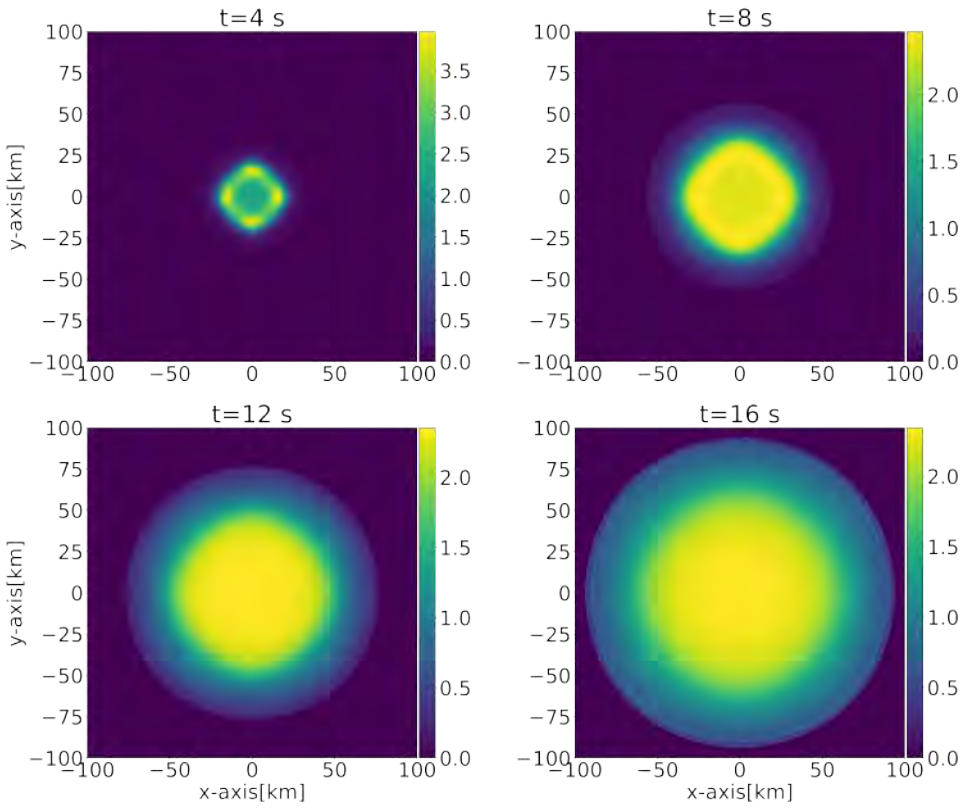


FIG. 7. Snapshots of the local energy ratio $E^S(\mathbf{r},t)/E^P(\mathbf{r},t)$ for the double couple simulation. As in fig. 6, the local ratio reaches an equilibrium value of 2.34 within the expanding yellow circle.

$t = (4, 8, 12, 16)$ s. These figures show an inner ring corresponding to $S$ energy propagation and an outer ring corresponding to $P$ energy propagation. In both simulations the local ratio approaches a numerical value of 2.34 at $t = 16$ s within the expanding yellow circle centered around the peak of the Gaussian. As energy propagates outwards, it scatters and starts to equilibrate over the 2 available wave modes. Fig. 6 shows that the area where the local ratio starts to converge towards $(\alpha_0/\beta_0)^2 = 2.34$ increases over time as the number of scattering events increase. However, the rate at which the local ratio converges to the theoretical value is a function of location, depending on the extent of scattering and on mode conversions. Fig. 7 shows a local behavior for the modal ratio for the double couple source

that is similar to that of the one in Fig. 6 for the pure $P$-source. Even though globally the mode equilibration occurs more quickly for the double couple source than for the explosive source (see fig. 4), locally that is not the case. After $t > 8$ s there is little difference in the local behavior of the modal equipartitioning between the two numerical simulations. The last panel in figs. 6 and 7 show that even though at very late times ($t = 16$ s) the global equipartitioning ratio is reached (see fig. 4), the local ratio is not yet reached for all locations behind the ballistic wave (i.e., only the locations within the exapnding yellow circle show a local ratio which approaches the global rati). Only in locations where the energy density is homogenized with enough scattering events, does the local ratio approach the theoretical value. The last panel of figs. 6 and 7 show that at locations close to the source (inner yellow ring), the local ratio approaches the theoretical value faster than for locations far from the source. For times much larger than for which we evolve the intensities, the local ratio eventually reaches $(\alpha_0/\beta_0)^2$, but it takes significantly longer than for the global ratio to reach the asymptotic value. For such propagation times, when the local ratio stabilizes, the energy distribution enters a locally equipartitioned state for the energy distribution between $P$ and $S$ modes.

### C. Angular Equipartitioning

For elastic waves, one usually considers the equipartitioning between wave modes, as energy equilibrates due to mode conversion (see figs. 4, 6 and 7). In addition to modal equilibration, angular equilibration occurs as the energy density homogenizes. Here, we numerically study the angular equipartitioning of the elastic energy as the number of

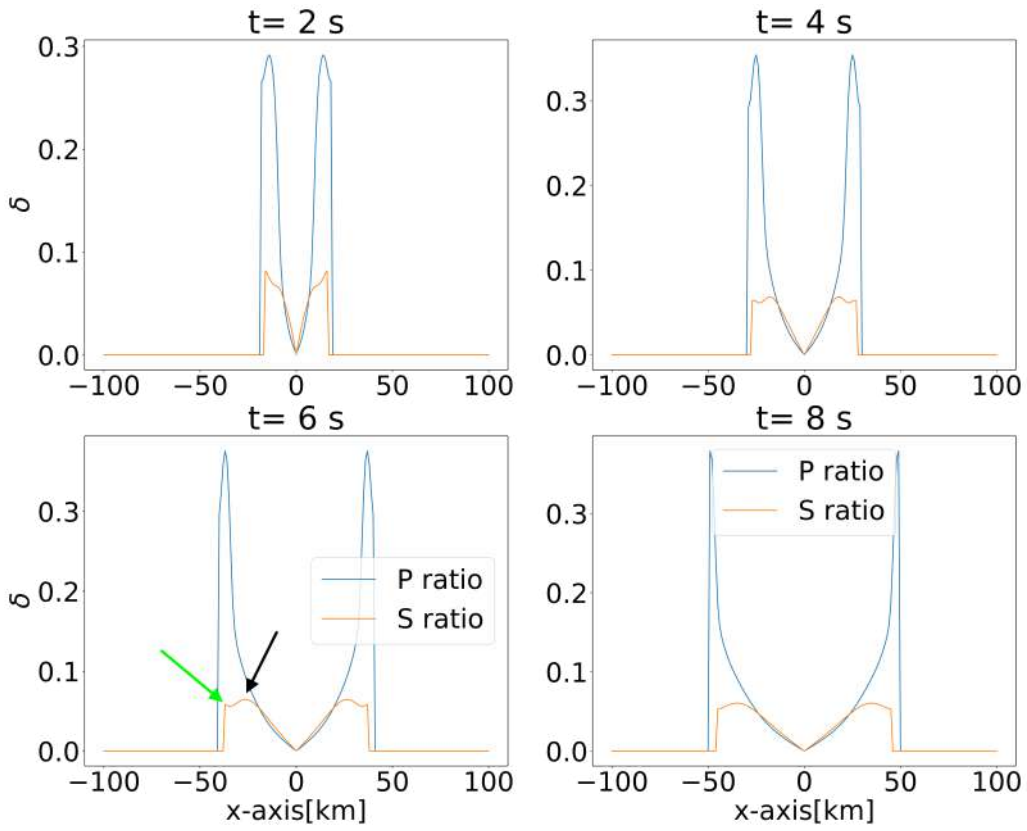


FIG. 8. Cross sections of the angular equipartitioning ratio $\delta$, for the pure $P$ source simulation, at $y = 0$ and $x \in [-100, 100]$ km. The green and black arrow point to two peaks that arise in $\delta_S$ due to mode conversion.

scattering events increase. To quantify the degree of angular equipartitioning we use the *equipartitioning index*, introduced by Jaimes and Snieder (2023),

$$\delta_{P,S}(\mathbf{r}, t) = \frac{\sigma_{P,S}(\mathbf{r}, t)}{\sqrt{N}\mu_{P,S}(\mathbf{r}, t)}, \tag{26}$$

where the subscript indicates $P$ or $S$ waves. In this expression $\sigma_{P,S}(\mathbf{r}, t)$ is the standard deviation of the $P$ or $S$ specific intensities along the angular directions defined with a division by $N - 1$, as $\sigma^2_{P,S}(\mathbf{r}, t) = \frac{1}{N-1}\sum_{i=1}^{N}(I_{P,S}(\mathbf{r}, t, \hat{\mathbf{n}}_i) - \mu_{P,S}(\mathbf{r}, t))^2$, while $\mu_{P,S}(\mathbf{r}, t) = \frac{1}{N}\sum_{i=1}^{N} I_{P,S}(\mathbf{r}, t, \hat{\mathbf{n}}_i)$ is the mean of the specific intensities along the angular direction, and

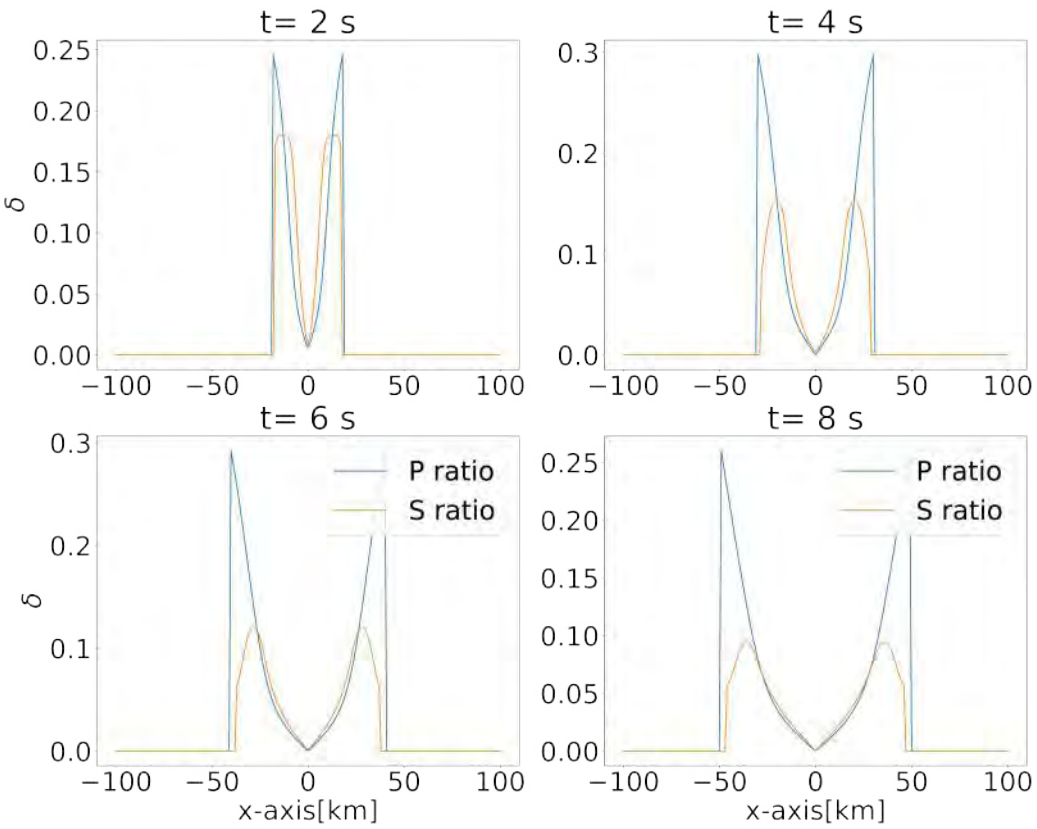


FIG. 9. Same as fig. 8, but for a double couple.

$N$ is the number of angular directions. The quantity $\delta_{P,S}$ provides a measure of the variation of the $P$ or $S$ specific intensities along the angular directions as a function of space and time. We compute the standard deviation and the mean of the specific intensities along the $N$ propagation directions for a fixed point in space and time. The constant $1/\sqrt{N}$ is included in eqn. 26 so that $0 \leq \delta_{P,S} \leq 1$. Consider an uni-directional intensity field $I_i = I_0 \delta_{i,1}$, where $I_0$ is the intensity along the only non-zero direction and $\delta_{i,j}$ is the Kronecher delta. The mean for this intensity field is $\mu = I_0/N$. The standard deviation for the same intensity field is $\sigma = I_0/\sqrt{N}$, which gives $\sigma/\mu = \sqrt{N}$. Hence, $\delta = 1$ for the most extreme case where all energy propagates in one direction. Thus, $\delta_{P,S} = 0$ when the intensity field $(P, S)$ is fully

equipartitioned in the angular sense (i.e., same specific intensity along all directions) and $\delta_{P,S} = 1$ when the intensity field is unidirectional (i.e., all of the specific intensities but one are equal to zero).

Figs. 8 and 9 show horizontal cross sections of the angular equipartitioning ratio $\delta_{P,S}$ at $y = 0$, of the explosive and double couple source simulations, respectively, for times $t = (2, 4, 6, 8)$ s. In the first simulation we release an explosive source with Gaussian spatial extent. Within this Gaussian we release the energy equally along all directions. Because of the nonzero gradient of the intensity field, part of the intensity propagates away from the initial Gaussian with a preferred propagation direction. As time progresses, this preferential propagation of the $P$ wave becomes more evident, as the increase in the value of the peaks of $\delta_P$ in fig. 8 shows. This figure shows that $\delta_P$ takes the highest value at the location of the ballistic wave. This value is significantly lower than one because of the spatial extent of the source (i.e., there is a preferrential direction but there is energy propagating in other directions). The value of $\delta_P$ decreases as one moves closer to the original source location centered at $x = 0$, where more scattering events have occurred relative to locations closer to the ballistic arrival. Some of this behavior also occurs with $\delta_S$. However, at times $t = 4$ s and $t = 6$ s there are two characteristic peaks in the equipartitioning index for $\delta_S$. The peak that is closer to the source (black arrow) corresponds to $P$ energy within the initial Gaussian that over time converts to $S$ energy. The peak that is further from the source (green arrow) corresponds to $S$ energy at time $t$ that propagates for most of the simulation (up to the current time $t$) as $P$ energy. This peak has a travel time that is close to that of the ballistic $P$ energy, and corresponds to single $P \rightarrow S$ scattering directly behind the

ballistic $P$ wave. Because of this scattering so close to the ballistic wave, the $S$ energy still has some preferred directionality and produces a maximum in $\delta_S$. Overall, the behavior of $\delta_{P,S}$ for the double couple simulation is similar to the one for the explosive simulation, with the exception of two differences. The first difference is that the highest value $\delta_P$ is slightly smaller than for the explosive source simulation. This is because this peak corresponds, not to $P$ ballistic energy, but to $P \rightarrow P$ energy conversion early in the simulation. The second difference is that the values of $\delta_S$ are larger than for the first simulation. This is because for the explosive source, all $S$-energy is caused by scattering (i.e., the source only releases $P$-energy). This means that for the explosive source, the $S$-waves are excited over a range of propagation directions as a consequence of mode conversion (see the radiation pattern for $P \rightarrow S$ scattering in fig. 1). For the double couple source there is a ballistic $S$-wave (unlike for the explosive source), which propagates at every point away from the source, and it is thus directional (higher $\delta_S$).

## IV. DISCUSSION

We developed a time-stepping algorithm for solving the elastic RTE in expressions 1 and 2. Our approach is based on first splitting the total intensity into the direct and scattered contributions, and then re-writing the RTE for the scattered intensities as integral equations. With these integral equations we evolve the specific $P$ and $S$ specific intensities over time, under the assumption that the time-step $\Delta t \ll \tau_p, \tau_s$ so that we can capture the scattering of $P$ and $S$ waves. Here, we disregard the boundary conditions, under the assumption that

for times less than the propagation time for a $P$-wave to reach the boundary, the boundary conditions do not influence the solution.

Contrary to many numerical developments, we resolve the angular distribution of both $P$ and $S$ energies. In our algorithm we discretize the angular integral and then handle the advection of $P$ and $S$ energy analytically at grid points and through interpolation within the numerical grid. This approach allows us to reduce dispersion errors as compared to standard numerical techniques such as finite differences or discontinuous Galerkin finite element methods. This numerical dispersion may cause negative intensities which are non-physical. To test the algorithm, we solve the RTE for both an explosive and a double couple source. We first benchmark our results against the diffusive approximation. After many scattering events this approximation is valid for any initial condition. Figs. 2 and 3 show that, at late times, our solutions match the diffusive approximation. The double couple source simulation takes longer to reach a diffusive state, compared to the explosive source simulation, because of the radiation pattern of the double couple. Since the double couple does not release energy in all possible directions, it takes a longer time, compared to the pure $P$ source, to redistribute the energy in all propagation directions. We test that the ratio between total $S$-wave energy to total $P$-wave energy converges to the global theoretical ratio $(\alpha_0/\beta_0)^2 = 2.25$ for the given choice of wave speeds. Fig. 4 shows that our simulations do indeed converge to the theoretical ratio, with the double couple simulation reaching it faster since at $t = 0$ the energy is already distributed among the two available wave modes. We also compare our numerical simulations to analytical expressions for the total energies $Y^P(t)$ and $Y^S(t)$ to validate the energy evolution throughout the simulation range. Fig 5

shows this comparison. Overall, our numerical results for the global equipartitioning ratio, the diffusive approximation, and the total energy as a function of time, match the known analytical expressions given by $\gamma_0^2$, eqn. A4 and eqn. B1, respectively. There is a small mismatch in the total energy at late times (fig. 5), which we can reduce by decreasing the value of $\Delta t$. We studied the local behavior of the energy equilibration between wave modes. Figs. 6 and 7 show that it takes significantly longer for the local equipartitioning to converge to the theoretical ratio, compared to the global ratio. As explained above, this is because for the local ratio to be established, the intensity field must be locally equipartitioned.

In addition to modal equipartitioning, we study angular equipartitioning. We use the equipartitioning index to study the angular randomization of the intensity fields. We find that, in general, the level of equipartitioning of an intensity field is a function of space and time. Figs. 8 and 9 show that the ballistic arrival has the highest equipartitioning index and that the trailing scattered energy becomes equipartitioned over time but not at the same rate throughout the computational domain. If we define $t_b$ as the arrival time of the ballistic wave, one can approximate the number of scattering events as $n \approx (t - t_b)/\tau_{av}$, where $\tau_{av}$ corresponds to a weighted average between the $P$ ($\tau_p$) and $S$ ($\tau_s$) scattering mean free times. For a given propagation time $t$, the larger $t_b$ is (greater distance), the smaller $n$ is. The algorithm that we introduce, together with our numerical simulations, allow us to study the propagation of $P$ and $S$ waves, and to investigate the local evolution of both modal and angular equipartitioning.

Our observations about the spatial and temporal dependence of equipartitioning have implications for the retrieval of Green's functions in seismic interferometry. The principle of

equipartition is regarded as a necessary, but not sufficient (Snieder *et al.*, 2010), condition to retrieve Green's functions. Because equipartition varies locally, depending on the extent of scattering, this implies that the accuracy with which one retrieves the Green's functions is also a function of space and time (Weaver, 2010).

## ACKNOWLEDGEMENTS

This work is supported by the Consortium Project on Seismic Inverse Methods for Complex Structures at the Colorado School of Mines.

## APPENDIX A: 2-D DIFFUSIVE APPROXIMATION

For a 3-D infinite medium, assuming there is no intrinsic attenuation, the diffusion approximation to the elastic RTE reads (Sato *et al.*, 2012)

$$E_{3d}(\mathbf{r},t) = \frac{W^P + W^S}{(4\pi D^*_{3d}t)^{3/2}} H(t) e^{-\frac{r^2}{4D^*_{3d}t}}, \tag{A1}$$

where $D^*_{3d}$ is the effective diffusion coefficient in 3-D, and $W^P$ and $W^S$ denote the $P$ and $S$ energy at $t = 0$, respectively. The diffusion coefficient is

$$D^*_{3d} = \frac{1}{3(1+2\gamma_0^3)}\left(\frac{\alpha_0}{g^{Pe}} + 2\gamma_0^3\frac{\beta_0}{g^{Se}}\right), \tag{A2}$$

where $\gamma_0 = \alpha_0/\beta_0$ is the ratio of mean $P$ wave speed to mean $S$ wave speed. $g^{Pe}$ and $g^{Se}$ are the $P$ and $S$ effective scattering coefficients. To obtain the diffusive approximation in 2-D we write the diffusion coefficient as

$$D^*_{2d} = \frac{1}{2(1+\gamma_0^2)}\left(\frac{\alpha_0}{g^{Pe}} + \gamma_0^2\frac{\beta_0}{g^{Se}}\right), \tag{A3}$$

where we replaced the 3-D equipartitioning ratio $2\gamma_0^3$ by its 2-D counterpart $\gamma_0^2$. We also replaced the factor 3 in the denominator of expression A2 by a factor 2, and replaced the exponent 3/2 in the denominator of eqn. A1 by the exponent 2/2, to account for the change from 3-D to 2-D (Snieder and Wijk, 2015). The diffusive approximation in 2-D reads

$$E_{2d}(\mathbf{r},t) = \frac{W^P + W^S}{(4\pi D^*_{2d} t)} H(t) e^{-\frac{r^2}{4D^*_{2d}t}}. \tag{A4}$$

## APPENDIX B: EXPRESSIONS FOR $Y^P(T)$ AND $Y^S(T)$

Sato *et al.* (2012) derive the following expressions for the total $P$ and $S$ energies in 3-D

$$\begin{aligned} Y^P(t) &= \frac{(g_0^{PS}\alpha_0 W^P - g_0^{SP}\beta_0 W^S)e^{-g_0^{PS}\alpha_0 t - g_0^{SP}\beta_0 t} + g_0^{SP}\beta_0(W^P + W^S)}{g_0^{PS}\alpha_0 + g_0^{SP}\beta_0}, \\ Y^S(t) &= \frac{(-g_0^{PS}\alpha_0 W^P + g_0^{SP}\beta_0 W^S)e^{-g_0^{PS}\alpha_0 t - g_0^{SP}\beta_0 t} + g_0^{PS}\alpha_0(W^P + W^S)}{g_0^{PS}\alpha_0 + g_0^{SP}\beta_0}. \end{aligned} \tag{B1}$$

To derive these expressions, Sato *et al.* (2012) make three assumptions. First, they assume that the source releases $P$ energy as $W^P\delta(\mathbf{r})\delta(t)$ and $S$ energy as $W^S\delta(\mathbf{r})\delta(t)$, where $W^P$ and $W^S$ are constants. Second, they assume that the angular dependence of the $P$ and $S$ specific intensities is small and almost isotropic. Third, they assume that the spatial gradient of both the $P$ and $S$ energy density vanishes at large distances from the source. If we define $W^P = \int \oint I_0^P(\mathbf{r},\theta) dx dy$ and $W^S = \int \oint I_0^S(\mathbf{r},\theta) d\theta dx dy$, and then assume that the gradient of both the $P$ and $S$ specific intensities vanishes at large distances from the source (without assuming that the $P$ and $S$ specific intensities are almost isotropic), the expressions in B1 remain valid. Expression B1 is valid in 2- and 3-D, with the scatteriing coefficients having a different definition depending on the dimension.

## APPENDIX C: CONSERVATION OF ENERGY

The choice of the parameters $A_{p,s}$ and $B_{p,s}$ in the linear system 20 determine the accuracy of the time stepping algorithm. To choose the values of $A_{p,s}$ and $B_{p,s}$ we impose energy conservation, so that the numerical algorithm conserves the energy as much as possible. We begin by re-defining expression 25 as

$$\begin{bmatrix} \vec{I}^P \\ \\ \vec{I}^S \end{bmatrix} = \begin{bmatrix} \boldsymbol{\eta}^{PP} & \boldsymbol{\eta}^{SP} \\ \\ \boldsymbol{\eta}^{PS} & \boldsymbol{\eta}^{SS} \end{bmatrix} \begin{bmatrix} \vec{W}^P \\ \\ \vec{W}^S \end{bmatrix}. \tag{C1}$$

We then write eqn. C1 as the following two equations

$$I^P(\mathbf{r}, \hat{\mathbf{n}}_j, t) = \sum_{i=1}^{N} \eta_{ji}^{PP} W^P(\mathbf{r}, \hat{\mathbf{n}}_i, t) + \sum_{i=1}^{N} \eta_{ji}^{SP} W^S(\mathbf{r}, \hat{\mathbf{n}}_i, t) \tag{C2}$$

$$I^S(\mathbf{r}, \hat{\mathbf{n}}_j, t) = \sum_{i=1}^{N} \eta_{ji}^{PS} W^P(\mathbf{r}, \hat{\mathbf{n}}_i, t) + \sum_{i=1}^{N} \eta_{ji}^{SS} W^S(\mathbf{r}, \hat{\mathbf{n}}_i, t). \tag{C3}$$

Adding equations C2 and C3 gives

$$I(\mathbf{r}, \hat{\mathbf{n}}_j, t) = \sum_{i=1}^{N} (\eta_{ji}^{PP} + \eta_{ji}^{PS}) W^P(\mathbf{r}, \hat{\mathbf{n}}_i, t) + \sum_{i=1}^{N} (\eta_{ji}^{SP} + \eta_{ji}^{SS}) W^S(\mathbf{r}, \hat{\mathbf{n}}_i, t). \tag{C4}$$

Summing both sides of equation C4 from $j = 1$ to $N$, and multiplying by $2\pi/N$ gives

$$I(\mathbf{r}, t) = \frac{2\pi}{N} \sum_{j=1}^{N} (\eta_{ji}^{PP} + \eta_{ji}^{PS}) \sum_{i=1}^{N} W^P(\mathbf{r}, \hat{\mathbf{n}}_i, t) + \frac{2\pi}{N} \sum_{j=1}^{N} (\eta_{ji}^{SP} + \eta_{ji}^{SS}) \sum_{i=1}^{N} W^S(\mathbf{r}, \hat{\mathbf{n}}_i, t), \tag{C5}$$

where we assumed that the terms $\sum_{j=1}^{N} \eta_{ji}^{PP}, \sum_{j=1}^{N} \eta_{ji}^{PS}, \sum_{j=1}^{N} \eta_{ji}^{SP}, \sum_{j=1}^{N} \eta_{ji}^{SS}$ are independent of $i$, for sufficiently small $\Delta t$. To show that this assumption is valid consider the block matrix $\boldsymbol{A}$ in the linear system 20 and its corresponding inverse $\boldsymbol{A}^{-1}$. As before, we write $\boldsymbol{A} = \boldsymbol{I} + \boldsymbol{K}$. Then, we apply the matrix expansion $(\boldsymbol{I} - \boldsymbol{K})^{-1} \approx \boldsymbol{I} + \boldsymbol{K}$, which is valid for $||\boldsymbol{K}|| \ll 1$.

With this expansion the elements of $\boldsymbol{A}^{-1}$ are

$$\eta_{ij}^{PP} = \delta_{ij} + \alpha_0 B_p \frac{2\pi}{N} \Delta t g_{pp}(\hat{\mathbf{n}}_i, \hat{\mathbf{n}}_j);\ \eta_{ij}^{SP} = \beta_0 B_p \frac{2\pi}{N} \Delta t g_{sp}(\hat{\mathbf{n}}_i, \hat{\mathbf{n}}_j)$$
$$\eta_{ij}^{PS} = \alpha_0 B_s \frac{2\pi}{N} \Delta t g_{ps}(\hat{\mathbf{n}}_i, \hat{\mathbf{n}}_j);\ \eta_{ij}^{SS} = \delta_{ij} + \beta_0 B_s \frac{2\pi}{N} \Delta t g_{ss}(\hat{\mathbf{n}}_i, \hat{\mathbf{n}}_j), \tag{C6}$$

which gives $\sum_{j=1}^{N}(\eta_{ji}^{PP} + \eta_{ji}^{PS}) = 1 + \alpha_0 B_p \Delta t g_{pp}^0 + \alpha_0 B_s \Delta t g_{ps}^0$ and $\sum_{j=1}^{N}(\eta_{ji}^{SP} + \eta_{ji}^{SS}) = 1 + \beta_0 B_p \Delta t g_{sp}^0 + \beta_0 B_s \Delta t g_{ss}^0$, justifying our assumption that the terms $\sum_{j=1}^{N} \eta_{ji}^{PP}, \sum_{j=1}^{N} \eta_{ji}^{PS}, \sum_{j=1}^{N} \eta_{ji}^{SP}, \sum_{j=1}^{N} \eta_{ji}^{SS}$ are independent of $i$, for sufficiently small $\Delta t$. We re-write the definitions for $W^P$ and $W^S$ from eqns. C7 and C8 to include both the direct and scattered energy as

$$\begin{aligned}\vec{W}_{tot}^{P}(\mathbf{r}, \hat{\mathbf{n}}, t) &= I^P(\mathbf{r} - \alpha_0 \Delta t \hat{\mathbf{n}}, \hat{\mathbf{n}}, t - \Delta t) e^{-\Delta t \alpha_0 (g_{pp}^0 + g_{ps}^0)} \\ &+ A_p \Delta t \frac{2\pi}{N} \sum_{\hat{\mathbf{n}}'} \Big[ \alpha_0 g_{pp}(\hat{\mathbf{n}}, \hat{\mathbf{n}}') I^P(\mathbf{r} - \alpha_0 \Delta t \hat{\mathbf{n}}, \hat{\mathbf{n}}', t - \Delta t) \\ &+ \beta_0 g_{sp}(\hat{\mathbf{n}}, \hat{\mathbf{n}}') I^S(\mathbf{r} - \alpha_0 \Delta t \hat{\mathbf{n}}, \hat{\mathbf{n}}', t - \Delta t) \Big] e^{-\Delta t \alpha_0 (g_{pp}^0 + g_{ps}^0)},\end{aligned} \tag{C7}$$

$$\begin{aligned}\vec{W}_{tot}^{S}(\mathbf{r}, \hat{\mathbf{n}}, t) &= I^S(\mathbf{r} - \beta_0 \Delta t \hat{\mathbf{n}}, \hat{\mathbf{n}}, t - \Delta t) e^{-\Delta t \beta_0 (g_{ss}^0 + g_{sp}^0)} \\ &+ A_s \Delta t \frac{2\pi}{N} \sum_{\hat{\mathbf{n}}'} \Big[ \beta_0 g_{ss}(\hat{\mathbf{n}}, \hat{\mathbf{n}}') I^S(\mathbf{r} - \beta_0 \Delta t \hat{\mathbf{n}}, \hat{\mathbf{n}}', t - \Delta t) \\ &+ \alpha_0 g_{ps}(\hat{\mathbf{n}}, \hat{\mathbf{n}}') I^P(\mathbf{r} - \beta_0 \Delta t \hat{\mathbf{n}}, \hat{\mathbf{n}}', t - \Delta t) \Big] e^{-\Delta t \beta_0 (g_{ss}^0 + g_{sp}^0)},\end{aligned} \tag{C8}$$

We Taylor-expand the specific intensities in eqn. C5 to first order around $(x, y, t - \Delta t)$, and integrate over space to obtain, with the help of the vanishing boundary conditions, the following system of equations

$$\begin{bmatrix} \eta_0^P(B_p, B_s)\alpha_0 \Delta t g_{pp}^0 e^{-\Delta t/\tau_p} & \eta_0^S(B_p, B_s)\alpha_0 \Delta t g_{ps}^0 e^{-\Delta t/\tau_s} \\ \eta_0^P(B_p, B_s)\beta_0 \Delta t g_{sp}^0 e^{-\Delta t/\tau_p} & \eta_0^S(B_p, B_s)\beta_0 \Delta t g_{ss}^0 e^{-\Delta t/\tau_s} \end{bmatrix} \begin{bmatrix} A_p \\ A_s \end{bmatrix} = \begin{bmatrix} 1 - \eta_0^P e^{-\Delta t/\tau_p} \\ 1 - \eta_0^S e^{-\Delta t/\tau_s} \end{bmatrix}, \tag{C9}$$

where $\eta_0^P(B_p, B_s) = \sum_{j=1}^{N}(\eta_{ji}^{PP}(B_p, B_s) + \eta_{ji}^{PS}(B_p, B_s))$, $\eta_0^S(B_p, B_s) = \sum_{j=1}^{N}(\eta_{ji}^{SP} + \eta_{ji}^{SS})$, $\tau_p = 1/(\alpha_0(g_{pp}^0 + g_{ps}^0))$, $\tau_s = 1/(\beta_0(g_{sp}^0 + g_{ss}^0))$. Notice that the matrix in expression C9 is a function of $B_p$ and $B_s$. Using $A_p + B_p = 1$ and $A_s + B_s = 1$, the solution vector in equation C9 is $[A_p, A_s] = [1/2, 1/2]$; hence we obtain $[B_p, B_s] = [A_p, A_s] = [1/2, 1/2]$, which corresponds to the trapezoidal rule.

Abdoulaev, G. S. (**2003**). "Three-dimensional optical tomography with the equation of radiative transfer," Journal of Electronic Imaging **12**(4), 594–601.

Aki, K., and Richards, P. G. (**2009**). *Quantitative seismology*, 2. edition, corrected printing ed. (University Science Books, Mill Valley, California New York).

Aumann, H. H., Chen, X., Fishbein, E., Geer, A., Havemann, S., Huang, X., Liu, X., Liuzzi, G., DeSouza-Machado, S., Manning, E. M., Masiello, G., Matricardi, M., Moradi, I., Natraj, V., Serio, C., Strow, L., Vidot, J., Chris Wilson, R., Wu, W., Yang, Q., and Yung, Y. L. (**2018**). "Evaluation of radiative transfer models with clouds," Journal of Geophysical Research: Atmospheres **123**(11), 6142–6157.

Baes, M., and Dejonghe, H. (**2001**). "Radiative transfer in disc galaxies - I. A comparison of four methods to solve the transfer equation in plane-parallel geometry," Monthly Notices of the Royal Astronomical Society **326**(2), 722–732.

Camps, P., and Baes, M. (**2018**). "The failure of Monte Carlo radiative transfer at medium to high optical depths," The Astrophysical Journal **861**(2), 80–89.

Chandrasekhar, S. (**1960**). *Radiative transfer* (Dover Publications, New York).

Clarke, P., Wang, H., Garrard, J., Abedi, R., and Mudaliar, S. (**2019**). "Space-angle discontinuous Galerkin method for plane-parallel radiative transfer equation," Journal of Quantitative Spectroscopy and Radiative Transfer **233**, 87–98.

de Abreu, M. P. (**2004**). "A two-component method for solving multislab problems in radiative transfer," Journal of Quantitative Spectroscopy and Radiative Transfer **85**(3-4), 311–336.

Dinther, C., Margerin, L., and Campillo, M. (**2021**). "Implications of laterally varying scattering properties for subsurface monitoring with coda wave sensitivity kernels: Application to volcanic and fault zone setting," Journal of Geophysical Research: Solid Earth **126**(12).

Duran, A., Planès, T., and Obermann, A. (**2020**). "Coda-wave decorrelation sensitivity kernels in 2-D elastic media: a numerical approach," Geophysical Journal International **223**(2), 934–943.

Evans, K. F., and Stephens, G. L. (**1995**). "Microwave radiative transfer through clouds composed of realistically shaped ice crystals. Part II. Remote sensing of ice clouds," Journal of the Atmospheric Sciences **52**(11), 2058–2072.

Fan, Y., An, J., and Ying, L. (**2019**). "Fast algorithms for integral formulations of steady-state radiative transfer equation," Journal of Computational Physics **380**, 191–211.

Francis, P. N., Cooke, M. C., and Saunders, R. W. (**2012**). "Retrieval of physical properties of volcanic ash using Meteosat. A case study from the 2010 Eyjafjallajökull eruption: Meteosat volcanic ash retrievals," Journal of Geophysical Research: Atmospheres **117**(D20).

Gaebler, P. J., Eulenfeld, T., and Wegler, U. (**2015**). "Seismic scattering and absorption parameters in the W-Bohemia/Vogtland region from elastic and acoustic radiative transfer theory," Geophysical Journal International **203**(3), 1471–1481.

Golub, G. H., and Van Loan, C. F. (**2013**). Johns Hopkins studies in the mathematical sciences *Matrix computations*, fourth edition ed. (The Johns Hopkins University Press, Baltimore), oCLC: ocn824733531.

Han, W., Huang, J., and Eichholz, J. A. (**2010**). "Discrete-ordinate discontinuous Galerkin methods for solving the radiative transfer equation," SIAM Journal on Scientific Computing **32**(2), 477–497.

Hennino, R., Trégourès, N., Shapiro, N. M., Margerin, L., Campillo, M., van Tiggelen, B. A., and Weaver, R. L. (**2001**). "Observation of Equipartition of Seismic Waves," Physical Review Letters **86**(15), 3447–3450.

Hofmeister, A. (**2005**). "Dependence of diffusive radiative transfer on grain-size, temperature, and Fe-content: implications for mantle processes," Journal of Geodynamics **40**(1), 51–72.

Iwabuchi, H. (**2006**). "Efficient Monte Carlo methods for radiative transfer modeling," Journal of the Atmospheric Sciences **63**(9), 2324–2339.

Jaimes, M. A., and Snieder, R. (**2023**). "Illustration of diffusion and equipartitioning as local processes: A numerical study using the radiative transfer equations," Submitted to The Journal of the Acoustical Society of America .

Kanu, C., and Snieder, R. (**2015**). "Numerical computation of the sensitivity kernel for monitoring weak changes with multiply scattered acoustic waves," Geophysical Journal

505 International **203**(3), 1923–1936.

506 Khazaie, S., Cottereau, R., and Clouteau, D. (**2017**). "Numerical observation of the
507 equipartition regime in a 3D random elastic medium, and discussion of the limiting
508 parameters," Computers & Geosciences **102**, 56–67.

509 Klose, A. D., and Hielscher, A. H. (**1999**). "Iterative reconstruction scheme for optical
510 tomography based on the equation of radiative transfer," Medical Physics **26**(8), 1698–
511 1707.

512 Klose, A. D., Netz, U., Beuthan, J., and Hielscher, A. H. (**2002**). "Optical tomography using
513 the time-independent equation of radiative transfer — Part 1: forward model," Journal of
514 Quantitative Spectroscopy and Radiative Transfer **72**(5), 691–713.

515 Le Hardy, D., Favennec, Y., and Rousseau, B. (**2016**). "Solution of the 2-D steady-state
516 radiative transfer equation in participating media with specular reflections using SUPG
517 and DG finite elements," Journal of Quantitative Spectroscopy and Radiative Transfer
518 **179**, 149–164.

519 Lee, K. H., Wong, M. S., Chung, S.-R., and Sohn, E. (**2014**). "Improved volcanic ash
520 detection based on a hybrid reverse absorption technique," Atmospheric Research **143**,
521 31–42.

522 Manners, J., Thelen, J.-C., Petch, J., Hill, P., and Edwards, J. (**2009**). "Two fast radiative
523 transfer methods to improve the temporal sampling of clouds in numerical weather
524 prediction and climate models: Fast RT methods for temporal sampling of clouds,"
525 Quarterly Journal of the Royal Meteorological Society **135**(639), 457–468.

Margerin, L., Campillo, M., and Van Tiggelen, B. (**2000**). "Monte Carlo simulation of multiple scattering of elastic waves," Journal of Geophysical Research: Solid Earth **105**(B4), 7873–7892.

Margerin, L., Planès, T., Mayor, J., and Calvet, M. (**2016**). "Sensitivity kernels for coda-wave interferometry and scattering tomography: theory and numerical evaluation in two-dimensional anisotropically scattering media," Geophysical Journal International **204**(1), 650–666.

Narayanan, D., Turk, M. J., Robitaille, T., Kelly, A. J., McClellan, B. C., Sharma, R. S., Garg, P., Abruzzo, M., Choi, E., Conroy, C., Johnson, B. D., Kimock, B., Li, Q., Lovell, C. C., Lower, S., Privon, G. C., Roberts, J., Sethuram, S., Snyder, G. F., Thompson, R., and Wise, J. H. (**2021**). "Powderday: Dust radiative transfer for galaxy simulations," The Astrophysical Journal Supplement Series **252**(1), 12–29.

Noebauer, U. M., and Sim, S. A. (**2019**). "Monte Carlo radiative transfer," Living Reviews in Computational Astrophysics **5**(1), 1–103.

Obermann, A., Planès, T., Hadziioannou, C., and Campillo, M. (**2016**). "Lapse-time-dependent coda-wave depth sensitivity to local velocity perturbations in 3-D heterogeneous elastic media," Geophysical Journal International **207**(1), 59–66.

Ostashev, V. E., Muhlestein, M. B., and Wilson, D. K. (**2017**). "Radiative transfer formulation for forest acoustics," The Journal of the Acoustical Society of America **142**(6), 3767–3780.

Paasschens, J. C. J. (**1997**). "Solution of the time-dependent Boltzmann equation," Physical Review E **56**(1), 1135–1141.

548 Pacheco, C., and Snieder, R. (**2005**). "Time-lapse travel time change of multiply scattered
549 acoustic waves," The Journal of the Acoustical Society of America **118**(3), 1300–1310.
550 Planès, T., Larose, E., Margerin, L., Rossetto, V., and Sens-Schönfelder, C. (**2014**).
551 "Decorrelation and phase-shift of coda waves induced by local changes: multiple scattering
552 approach and numerical validation," Waves in Random and Complex Media **24**(2), 99–125.
553 Prata, A. J. (**1989**). "Infrared radiative transfer calculations for volcanic ash clouds,"
554 Geophysical Research Letters **16**(11), 1293–1296.
555 Przybilla, J., and Korn, M. (**2008**). "Monte Carlo simulation of radiative energy transfer
556 in continuous elastic random media-three-component envelopes and numerical validation,"
557 Geophysical Journal International **173**(2), 566–576.
558 Przybilla, J., Korn, M., and Wegler, U. (**2006**). "Radiative transfer of elastic waves versus
559 finite difference simulations in two-dimensional random media," Journal of Geophysical
560 Research **111**(B4), B04305.
561 Quijano, J. E., and Zurk, L. M. (**2009**). "Radiative transfer theory applied to ocean bottom
562 modeling," The Journal of the Acoustical Society of America **126**(4), 1711–1723.
563 Reboul, E., Le Bot, A., and Perret-Liaudet, J. (**2005**). "Radiative transfer equation for
564 multiple diffraction," The Journal of the Acoustical Society of America **118**(3), 1326–1334.
565 Ren, K., Abdoulaev, G. S., Bal, G., and Hielscher, A. H. (**2004**). "Algorithm for solving the
566 equation of radiative transfer in the frequency domain," Optics Letters **29**(6), 578–580.
567 Roberge, W. G. (**1983**). "The spherical harmonics solution for the radiation field in plane-
568 parallel clouds with embedded sources," The Astrophysical Journal **275**, 292–306.

569 Rossetto, V., Margerin, L., Planès, T., and Larose, r. (**2011**). "Locating a weak change
570 using diffuse waves: Theoretical approach and inversion procedure," Journal of Applied
571 Physics **109**(3), 034903.

572 Sato, H., Fehler, M. C., and Maeda, T. (**2012**). *Seismic Wave Propagation and Scattering in*
573 *the Heterogeneous Earth : Second Edition* (Springer Berlin Heidelberg, Berlin, Heidelberg).

574 Sato, H., Nakahara, H., and Ohtake, M. (**1997**). "Synthesis of scattered energy density for
575 nonspherical radiation from a point shear-dislocation source based on the radiative transfer
576 theory," Physics of the Earth and Planetary Interiors **104**(1), 1–13 stochastic Seismology
577 Stochastic Seismic Wave Fields and Realistic Media.

578 Sánchez-Sesma, F. J., Pérez-Ruiz, J. A., Luzón, F., Campillo, M., and Rodríguez-
579 Castellanos, A. (**2008**). "Diffuse fields in dynamic elasticity," Wave Motion **45**(5), 641–654.

580 Snieder, R. (**2002**). "Coda wave interferometry and the equilibration of energy in elastic
581 media," Physical Review E **66**(4), 046615.

582 Snieder, R., Duran, A., and Obermann, A. (**2019**). "Locating velocity changes in elastic
583 media with coda wave interferometry," in *Seismic ambient noise*, edited by N. Nakata,
584 L. Gualtieri, and A. Fichtner (Cambridge University Press, Cambridge, UK), pp. 188–217,
585 section: 6.

586 Snieder, R., Fan, Y., Slob, E., and Wapenaar, K. (**2010**). "Equipartitioning is not sufficient
587 for Green's function extraction," Earthquake Science **23**(5), 403–415.

588 Snieder, R., and Wijk, K. v. (**2015**). *A Guided Tour of Mathematical Methods for the*
589 *Physical Sciences*, 3 ed. (Cambridge University Press, Cambridge).

590 Steinacker, J., Bacmann, A., and Henning, T. (**2002**). "Application of adaptive
591 multi-frequency grids to three-dimensional astrophysical radiative transfer," Journal of
592 Quantitative Spectroscopy and Radiative Transfer **75**(6), 765–786.

593 Trégourès, N. P., and van Tiggelen, B. A. (**2002**). "Generalized diffusion equation for
594 multiple scattered elastic waves," Waves in Random Media **12**(1), 21–38.

595 Turner, J. A., and Weaver, R. L. (**1994**). "Radiative transfer of ultrasound," The Journal
596 of the Acoustical Society of America **96**(6), 3654–3674.

597 Weaver, R. L. (**1982**). "On diffuse waves in solid media," The Journal of the Acoustical
598 Society of America **71**(6), 1608–1609.

599 Weaver, R. L. (**2010**). "Equipartition and retrieval of Green's function," Earthquake Science
600 **23**(5), 397–402.

601 Wolf, S. (**2003**). "Efficient Radiative Transfer in Dust Grain Mixtures," The Astrophysical
602 Journal **582**(2), 859–868.

603 Wu, R. S., and Aki, K. (**1985**). "Elastic wave scattering by a random medium and the
604 small-scale inhomogeneities in the lithosphere," Journal of Geophysical Research **90**(B12),
605 10261.

606 Xu, F., Davis, A. B., West, R. A., Martonchik, J. V., and Diner, D. J. (**2011**). "Markov
607 chain formalism for vector radiative transfer in a plane-parallel atmosphere overlying a
608 polarizing surface," Optics Letters **36**(11), 2083–2085.

609 Yamamoto, M., and Sato, H. (**2010**). "Multiple scattering and mode conversion revealed by
610 an active seismic experiment at asama volcano, japan," Journal of Geophysical Research:
611 Solid Earth **115**(B7).

Yodh, A., and Chance, B. (**1995**). "Spectroscopy and imaging with diffusing light," Physics Today **48**(3), 34–40.

Yoshimoto, K. (**2000**). "Monte Carlo simulation of seismogram envelopes in scattering media," Journal of Geophysical Research: Solid Earth **105**(B3), 6153–6161.

Zhang, T., and Sens-Schönfelder, C. (**2022**). "Adjoint envelope tomography for scattering and absorption using radiative transfer theory," Geophysical Journal International **229**(1), 566–588.

Zhang, T., Sens-Schönfelder, C., and Margerin, L. (**2021**). "Sensitivity kernels for static and dynamic tomography of scattering and absorbing media with elastic waves: a probabilistic approach," Geophysical Journal International **225**(3), 1824–1853.